Feasibility of Rocket Artillery Systems With Reusable First Stage

Mikhail V. Shubov
University of MA Lowell
One University Ave,
Lowell, MA 01854
E-mail: viktor_shubov@uml.edu

Abstract

A concept of guided artillery rockets with reusable first stage otherwise called a rocket launcher aircraft (RLA) is presented. RLA raises the second stage rockets (SSR) to an altitude of up to 20 *km*. While RLA is moving at low supersonic speed, it releases one or more SSRs. RLA returns to the base within a few minutes of it's launch. SSRs use slow burning motors to gain altitude and velocity. At the apogee of their flight SSRs release projectiles which fly to the target and strike it at high impact velocity. The projectiles reach a target at ranges of up to 374 *km* and impact velocity up to 1.35 km/s. We show that a rocket launched at high altitude and high initial velocity does not need expensive thermal protection to survive ascent. Delivery of munitions to target by the system described should be much less expensive than delivery by a conventional rocket. All parameters of RLA, SSR, and their trajectories are calculated based on theoretical (mechanical and thermodynamical) analysis and on several MatLab programs.

Introduction

In this work we discuss a possibility of a long range two-stage artillery rocket system with a reusable first stage. The first stage will be referred to as Rocket Launcher Aircraft (RLA). RLA is itself a rocket-powered aircraft which raises the Second Stage Rockets (SSR) to an altitude of 12 *km* – 20 *km* and fires them with the initial speed of 500 m/s – 700 m/s relative to the ground. Then RLA returns to its base ready for refuelling and another sortie.

The SSR is an expendable rocket. It has a slow-burning motor which burns 60 *s* – 80 *s*. After the SSR motor burns out, it follows a ballistic trajectory. As the SSR reaches the apogee of 77 *km* – 111 *km*, it releases one or more warheads which fly to the target. The SSR itself burns up in the atmosphere a few *km* away from the target. Delivery of payload to target should be less expensive than conventional rocket systems.

It may be noticed that conventional fighters and bombers also deliver munitions to a relatively long distance at a relatively low price. Unlike RLA, conventional fighters and bombers expose themselves to antiaircraft fire, which may make their operations inefficient. RLA never flies into hostile territory.

The current work consists of 5 Sections. In Section 1, we describe the state of the art rocket systems capable of making precise strikes to the range of 80 km to 600 km also mentioning some longer range missiles. In Tables 1 and 2, we present the cost of delivery per kg of payload. For ranges of 156 km to 600 km, the costs are from $ 2,700 per kg to $ 6,700 per kg depending on the missile. Thus we establish the need for a less expensive system.

In Section 2, we introduce the physics of rocket flight. We present the equations describing the rocket trajectory. We also introduce the concept of Specific Impulse – an important concept for rocket development. The material in Section 2 is used to write programs and perform calculations with results presented in subsequent sections.

In Section 3, we discuss rockets using solid and liquid propellants. For solid propellants we present properties of several fuel compositions. We discuss possible fuel grain shapes. We also discuss different rocket container materials along with their corresponding advantages and disadvantages. We present possible choices of liquid propellants and oxidizers. Some combinations are hypergolic – they ignite upon contact. We also present liquid fuel prices.

In Section 4, we discuss the RLA, which is presented in Fig. 7. A 7 min 20 sec sortie is described in Subsection 4.1. In Subsections 4.2 and 4.3 we describe exotic engines which can be used as auxiliary engines for RLA: rocketprop and air turborocket.

In Section 5, we calculate rocket performance. In Subsection 5.1 we calculate the maximum mass of SSR, which can be carried by a RLA. That mass is 4.3% to 12.6% of fuelled RLA liftoff mass depending on sortie requirements. In Subsection 5.2 we describe the performance of artillery rockets fired from RLA. In Subsection 5.3 we calculate the impact velocity of several projectiles. Europrojectile is a small tungsten projectile described in Subsubsection 5.3.2. It has the best performance.

In Section 6, we describe the aerodynamic heating by laminar and turbulent air flows. In Subsection 6.1 we present the general expressions for aerodynamic heating of different parts of the rocket. The material in Subsection 6.1 is used to write programs and perform calculations with the results presented in Subsection 6.3. In Subsection 6.2 we discuss the heat shields. In Subsection 6.3 we calculate the heating rates and temperatures of different parts of SSR during flight.

An artillery rocket has a diameter of 30 cm, total mass 300 kg, and a nose cone warhead compartment with a mass of 70 kg. It burns 60 to 80 seconds. It releases the warheads at the apogee. Fired from 12 km altitude with an initial velocity of 500 m/s, it has a range of 263 km. In this case the impact velocity of the Europrojectile is 1,150 m/s. Fired from 16 km altitude with an initial velocity of 600 m/s, it has a range of 318 km. In this case the impact velocity of the Europrojectile is 1,241 m/s. Fired from 20 km altitude with an initial velocity of 700 m/s, it has a range of 374 km. In this case the impact velocity of the Europrojectile is 1,349 m/s.

In Section 7, we present a conclusion. We also describe other possible artillery systems with reusable or mostly reusable first stage.

In the conclusion of the Introduction, for reader's convenience, we provide a list of abbreviations used in the text, and a list of chemical notations.

List of Abbreviations – General

ATACMS – army tactical missile system (USA)
ATR – air turborocket

CEP – circular error probability
DF – Dong-Feng ballistic missiles (China)
GMLRS – guided multiple launch rocket system (USA)
HPV – hypervelocity projectile
JDAM – joint direct attack munition (guidance kit for any bomb)
LORA – long range attack missile (Israel)
MLRS – multiple launch rocket system
PGK – precision guidance kit
RASAero – aerodynamic analysis and flight simulation software
RLA – rocket launcher aircraft
RPA – rocket propulsionanalysis
SSR – second stage rocket
TBM – theatre ballistic missile
VTVL – vertical takeoff, vertical landing

List of Abbreviations – Chemicals

AP – ammonium perchlorate
AN – ammonium nitrate
EEC — the mixture of 61% monoethanolamine, 30% ethanol, and 9% hydrated copper nitrate
ETA — the mixture of ethanolamine and 10% $CuCl_2$
ETAFA — the mixture of 47.5% Ethanolamine, 47.5% Furfuryl Alcohol, and 5.0% $CuCl_2$
HP95 – 95% hydrogen peroxide
HTPB – hydroxyl-terminated polybutadiene
LO2 – liquid oxygen
NG – nitroglycerin
RFNA – red fuming nitric acid – 79% $HN0_3$ and 19% N_2O_4

1 State of the Art Rocket Artillery

1.1 Artillery Rockets

Short range ballistic missiles can make precise strikes at ranges from 150 *km* to 1,000 *km*. Some of the modern systems are extremely expensive. Cost per 1 *kg* of munitions delivered to the target varies between $1,500 and $10,000 depending on the range.

Scud missile was the original Soviet short range ballistic missile. Scud-A introduced in 1957 delivered a 950 *kg* payload to a range of 180 *km*. Scud-B introduced in 1964 delivered a 985 *kg* payload to a range of 300 *km*. Over 7,000 Scud-B missiles have been built. Scud-C introduced in 1965 delivered a 600 *kg* payload to a range of 600 *km*. Scud-D introduced in 1989 delivered a 985 *kg* payload to a range of 700 *km*. Scud missiles have been used extensively in *Iran-Iraq War*. Between October 1988 and February 1992 approximately 1,700 to 2,000 Scud missiles were launched in Afghanistan's civil war [1]. Original Scud missiles had poor guidance, but in modern times, relatively inexpensive and precise guidance systems are available. Russian theatre rocket

Iskander delivers a 480 *kg* payload to a distance of 500 *km* or a 700 *kg* unit to a distance of 400 *km*. The missile has very precise guidance. Russia has only 136 such missiles. The price is kept secret, but should be at least $4 Million per unit [2, p.125].

American theatre rocket ATACMS delivers a 230 *kg* payload to 300 *km* or a 560 *kg* payload to 165 *km*. The missile has very precise guidance. USA has 3,700 units [3]. The unit cost of ATACMS is $1.5 Million [4, p.19]. Israel has developed LORA ("Long Range Attack") missile, which delivers a 570 *kg* payload to a distance of 400 *km*. The missile has very precise guidance. The unit cost is not disclosed [5].

China has Dong-Feng ballistic missiles. Some of these missiles are intercontinental ballistic missiles. Main short-range ballistic missiles are DF-11 and DF-15. DF-11 launches an 800 *kg* payload to a range of 280 *km* or a 500 *kg* payload to a range of 350 *km*. DF-11A launches an 500 *kg* payload to a range of 350 *km*. DF-15 launches an 500 *kg* payload to a range of 600 *km*. DF-15A launches an 600 *kg* payload to a range of 600 *km*. DF-15B launches an 600 *kg* payload to a range of 700 *km* [6, p.48]. China possesses about 1,200 ballistic rockets with ranges 300 *km* to 1,000 *km* [7, p.31].

Artillery rockets can deliver guided submunitions much better than artillery projectiles, since they are not subject to extreme accelerations. Guided Multiple Launch Rocket System (GMLRS) is used by USA. M30 and M31 rockets deliver a 90 *kg* payload to 84 *km*. The missile has very precise guidance [8, p.112]. By 2014, 19,942 GMLRS rockets have been procured at a cost of $125,850 per rocket. During the years 2014-2015, 2,940 GMLRS rockets have been procured at a cost of $400 Million [4, p.19] – which gives GMLRS rocket a unit price of $136,000. Smerch is a powerful Russian rocket artillery system. A single vehicle carries 12 rockets. A single rocket delivers a 243 *kg* warhead to a range of 90 *km* with great accuracy. Multiple Launch Rocket System (MLRS) Smerch has been used in *Second Chechen War*, *War in Donbass*, and *Syrian Civil War*. The unit price is undisclosed [9]. China has several powerful rocket artillery systems. AR3 is a 370 *mm* caliber rocket which delivers a 200 *kg* warhead to a range of 220 *km* with great accuracy. Each launcher has 8 rockets [10].

USA did use the rockets described above in recent local conflicts. Out of 17,184 GMLRS Unitary rockets produced, 3,141 have been used in Iraq and Afghanistan. Out of 1,650 Army Tactical Missile System (ATACMS) Block I rockets produced, 32 have been used in *Desert Storm* and 379 in *Operation Iraqi Freedom*. Out of 610 ATACMS Block IA rockets produced, 74 have been used in *Operation Iraqi Freedom*. Out of 176 ATACMS Quick Reaction Unitary rockets produced, 16 have been used in *Operation Iraqi Freedom* and 42 in *Operation Enduring Freedom*. Out of 513 ATACMS 2000 rockets produced, 33 have been used in *Operation Enduring Freedom* [11].

The measure of expense for a missile system at a given range is the cost per unit delivered weight. Below we tabulate the costs for the few solid propellant rockets for which the information is not classified:

Missile	Range	Throw weight	Unit Cost	Cost per *kg* delivered
GMLRS	84 *km*	90 *kg*	$ 136,000	$ 1,500
ATACMS	165 *km*	560 *kg*	$ 1,500,000	$ 2,700
ATACMS	300 *km*	230 *kg*	$ 1,500,000	$ 6,500
Trident II [12]	7,840 *km*	2,800 *kg*	$ 37,300,000	$ 13,300

Table 1: Solid propellant missiles

Liquid propellant rockets are less expensive, but they require about an hour to be prepared for firing. Some of them are listed in Table 2 below. The first two prices in 1990s are given in [13]. The prices listed below are double the old prices.

Missile	Range	Throw weight	Unit Cost	Cost per *kg* delivered
Dong-Feng 15	500 *km*	600 *kg*	$ 4,000,000	$ 6,700
Scud C	600 *km*	600 *kg*	$ 2,000,000	$ 3,300
Agni II [14]	2,000 *km*	1,000 *kg*	$ 5,100,000	$ 5,100

Table 2: Liquid propellant missiles

As can be seen from the above table, the cost of delivering munitions by short range ballistic missiles is very high. The costs of long range missiles are relatively low for their range.

1.2 Guided Munitions

One of the most important factors enabling long-range missiles and artillery is appearance and development of guided munitions. Precise guidance allows projectiles to strike targets tens or hundreds kilometers away with an accuracy of a few meters.

The most common guided munition is the air bomb. Guided bombs and glide bombs were first used by Germany in 1943 [15, p.4]. Since that time, relatively inexpensive guided bombs came into common use – during operations *Enduring Freedom* in 2001 and *Iraqi Freedom* in 2003, 80% of all bombs used were guided [16, p. 232]. Joint Direct Attack Munition (JDAM) is a guidance kit which can be attached to any unguided bomb in order to transfer it into a guided bomb [15, p.213]. "Through FY 2005, 105,286 JDAM kits had been procured for an average unit-procurement cost of $21,379 each" [15, p.217]. Recently the Boeing corporation has produced 300,000th JDAM [17]. Warheads used by the system we are proposing in this paper are similar to bombs dropped from an apogee of the second-stage rocket flight. They are much lighter than conventional bombs, but they will experience strong heating due to high velocity.

Guided projectiles and projectile guidance kits are much more hardy than bomb or missile guidance – they must survive acceleration of thousands of g's inside a cannon. Low cost guidance systems for cannon launched projectiles are becoming available [18]. The present generation of guided tube artillery munitions uses precision guidance kits attached to non-guided projectiles. The kit currently used by US Army is "M1156 Precision Guidance Kit (PGK)". PGK consists of a 1.5 *kg* fuse placed in the nose of a non-guided projectile. M1156 uses GPS guidance [19].

The projectile equipped with a fuse was suppose to have a circular error probability (CEP) of 30 *m* [20]. Almost always new technology performs below expected parameters with M1156 being a nice exception. “During its first lot acceptance testing in April 2015, the M1156 demonstrated median accuracy of less than 10 *m* with a reliability of 97% when fired from the 155 *mm*/39-calibre M109A6 Paladin." [21, p.8] A German test had even better result. "From a distance of 27 *km* percent of the PGK-equipped German shells landed within 5 meters of the target" [19]. PGK M1156 have a unit price of $10,000 [22].

In 2013, 1,300 PGKs have been delivered to US Armed Forces in Afghanistan. Australia has a contract with USA for 4,000 PGKs [23, p. 21]. By February 2017, 10,000 units have been produced [24]. By May 2018, 25,000 units have been produced [25]. One advantage of M1156 is it’s simplicity:

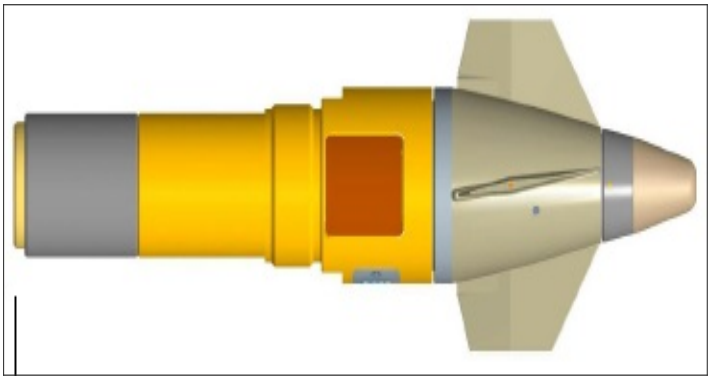

Figure 1: Projectile guidance kit [22]

> The kit has a
> single moving part, the canard assembly,which can only rotate along the longitudinal axis, the wings having a fixed cant; two couples of opposite wings have the same direction and thus provide lift, while the two despin wings provide counter-rotation. The assembly being coupled to an alternator, counter-rotation produces electrical power and initiates the battery [23, p. 21].

100,000 PGKs are ordered [21, p.8]. Israel is also developing a guidance kit called "Silver Bullet". The kit can be fitted to the nose of any conventional or rocket assisted projectile. This PGK does have four moving wings [23, p. 21-22]. Another guidance kit developed by Israel is TopGun [26]. Guidance kits used to guide projectiles should be able to guide warheads released by second-stage rockets.

The Hypervelocity Projectile (HPV) should be the next generation of guided munitions [27, p.12]. It’s guidance should easily survive extreme acceleration within a launcher and heating within atmosphere. The projectile’s guidance system should work even if it is shot from an electromagnetic cannon to a range of 400 *km*. HPV has a conical shape. It is made mostly out of tungsten. HPV’s weight is 11.4 *kg*, length 64.2 *cm*, and caliber 7.83 *cm*. It is shown in Figure 3 below:

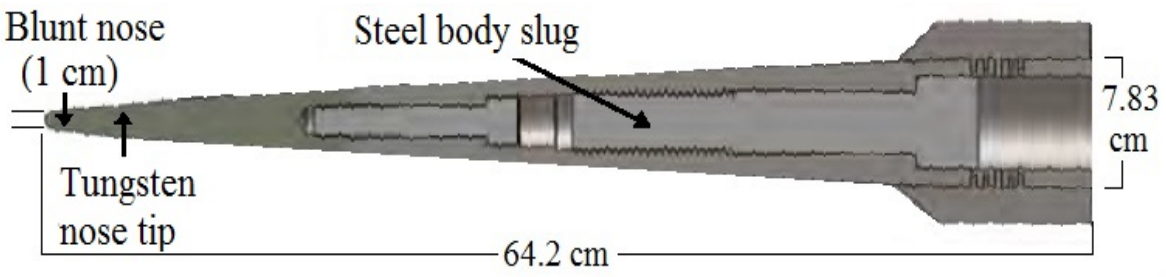

Figure 2: Hypervelocity projectile

HPV is very fit to be one of possible warheads carried by a second stage artillery rocket.

1.3 Rockets With Reusable First Stage

From the first space launches of the late 1950s until now, launching payload into orbit has been very expensive. The primary cost comes from the fact that until recently, no launch vehicle has been reusable. Propellant and oxidizer make up under 1% of space launch cost [28]. There have been many projects of reusable spaceships dating back at least to 1960s, but none of them have been successful [29, p. 12-13]. On December 21, 2015, Space X made a huge step in history, when the first stage of Falcon 9 spacecraft returned to the launching pad [29, p.1].

Currently Space X can deliver payload to Low Earth Orbit at \$4,530 per kg, which is much less expensive than the cost that can be suggested by other companies [29, p. 135, 140]. Space X plans to reduce that price to \$3,200 per kg in the near future [29, p. 156]. One Falcon 9 launch costs \$62 million, about \$300,000 of which is the cost of fuel [30]. Several other companies and national agencies have plans for producing their own space vehicles with a reusable first stage [31].

Reusability of space vehicles is still in its infancy. Full reusability would bring down the cost of space transportation by a great margin, which is still unknown. Reusable spacecraft would issue a dawn of Space Colonization and the beginning of the true Space Age.

In this work we discuss the application of rocketry with reusable first stage to military technology. This technology holds great potential for both military and civilian applications.

2 The Physics of Rocket Flight

This section describes the equations of motion of a rocket as well as aerodynamic heating it experiences. Equations for trajectory, velocity, and heating of the rocket are the same for the (RLA) and (SSR).

2.1 Rocket Motion

Let us consider a rocket that starts ascent at height h_0, which is generally from 12 km to 20 km, with the initial speed is v_0, which is generally 500 m/s to 700 m/s, with the angle with respect to horizontal line α_0, generally between 51^o and 68^o.

Three forces acting on a rocket during flight are presented in Figure 3. The gravitational force is $M(t)\mathbf{g}$ pointed in $-\hat{y}$ direction. Notice, that while the rocket fuel is burning, the rocket mass is decreasing. The air resistance or drag force $\mathbf{F}_d$ is acting in the opposite direction of velocity. The magnitude of F_d is

$$F_d = C_d(\mathscr{M})\frac{\rho v^2 A}{2} = C_d(\mathscr{M})\ \ \mathscr{M}^2\ \ \frac{\rho v_s^2 A}{2}, \tag{2.1}$$

where $C_d(\mathscr{M})$ is the Mach–number dependent drag coefficient, v is the velocity, v_s is the speed of sound, $\mathscr{M}$ is the Mach number, i.e. $\mathscr{M} = v/v_s$, ρ is the air density, and A is the base area of the rocket. Let M be the rocket mass. Then thrust force $\mathbf{F}_t$ acting in the direction of velocity is given by

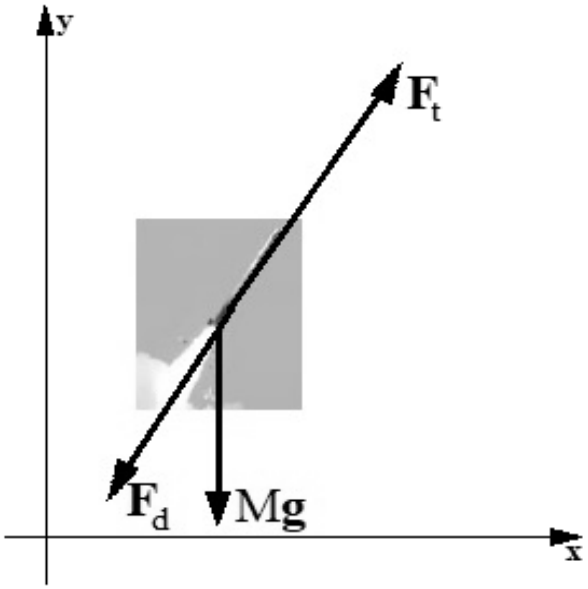

Figure 3: Forces acting on a firing rocket [32]

$$F_t = \dot{M} v_e, \tag{2.2}$$

where $\dot{M}$ is the fuel burning rate. For the SSR and pure rocket propulsion RLA, v_e is the exhaust velocity. For an air-breathing RLA, v_e is the **effective exhaust velocity**. Generally, the effective exhaust velocity of air-breathing engines is 8,000 m/s to 45,000 m/s. These effective velocities are not attained by any gas in these engines. Their actual jets have velocity of 500 m/s – 700 m/s.

For a pure rocket propulsion, v_e increases as the rocket rises out of dense atmospheric layers. For the SSR launched at a high altitude the exhaust velocity barely changes. For some propellant grains, the fuel burning rate changes during the burn time, while in our case we assume an almost steady burning rate

$$\dot{M} = \frac{M\ f_p}{t_b} \qquad \text{for time } \ 0 \le t \le t_b, \tag{2.3}$$

where t_b is the **burn time** and f_p is the **propellant mass fraction** given by

$$f_p = \frac{\text{Propellant mass}}{\text{Combined mass of propellant, rocket, and payload}}. \tag{2.4}$$

Since we know the forces acting on the rocket, we calculate its trajectory via the MatLab programs **FirstStage.m** and **Rocket.m** , which are described at the end of this Subsection.

The change in velocity produced by the rocket engine is

$$v_r = \int_0^{t_b} \frac{\mathbf{F}_t(t)}{M(t)}\, dt, \tag{2.5}$$

where $M(t)$ is the rocket mass at time t. According to *Tsialkovski Rocket Equation* [33],

$$v_r = -\bar{v}_e\ ln\big(1 - f_p\big), \tag{2.6}$$

where $\bar{v}_e$ is the average exhaust velocity. In our case, $\bar{v}_e \approx 2,100\ m/s$. For expensive rockets with flame temperatures in excess of 2,800 ^oC, $\bar{v}_e \approx 2,600\ m/s$.

The drag loss is

$$v_d = \int_0^{t_0} \frac{F_d(t)}{M(t)}\, dt, \tag{2.7}$$

where m is the projectile mass, t_0 is the time it takes the rocket to reach the apogee, and $F_d(t)$ is the drag force at the time moment t.

At this point we define the effective loss of rocket velocity due to gravity. It is called **gravitational loss** and denoted v_g. We define this loss in terms of the rocket's speed and altitude at the apogee. First, assume that the rocket is given it's impulse v_r instantaneously, and the drag loss is negligible. Such assumption is an abstract limit for a rocket, but it may be reality for a projectile fired at high altitude. Then the total kinetic and potential energy per unit rocket (projectile) mass at the beginning of trajectory is

$$\mathscr{E} = gh_0 + \frac{\left(v_0 + v_r\right)^2}{2}, \tag{2.8}$$

where h_0 is the launch altitude, v_0 is the launch velocity, and v_r is the velocity gain due to the action of the rocket engine. Second, we incorporate the aerodynamic drag loss into (2.8) to obtain

$$\mathscr{E} = gh_0 + \frac{\left(v_0 + v_r - v_d\right)^2}{2}, \tag{2.9}$$

where v_d is the drag loss. Third, we incorporate the gravitational loss into (2.9) to obtain

$$\mathscr{E} = gh_0 + \frac{\left(v_0 + v_r - v_d - v_g\right)^2}{2}, \tag{2.10}$$

where v_g is the gravitational loss. In the above expressions, v_0, v_r, v_d, and h_0 are known, while both $\mathscr{E}$ and v_g are unknown. In order to calculate v_g, we calculate $\mathscr{E}$ using the parameters of rocket motion at the apogee. The maximum ascent of the rocket, or the height the rocket attains at apogee is denoted h_A. The rocket speed at the apogee is v_A. The vector of this speed is in the forward direction. The total kinetic and potential energy per unit rocket mass at the apogee is

$$\mathscr{E} = gh_A + \frac{v_A^2}{2}, \tag{2.11}$$

which is the same as the rocket energy earlier in the path given in (2.10). Equating (2.10) and (2.11), we obtain

$$v_g = \left(v_0 + v_r\right) - v_d - \sqrt{2g\left(h_A - h_0\right) + v_A^2}. \tag{2.12}$$

The aforementioned program **FirstStage.m** performs calculations for the RLA. The user inputs RLA's mass, diameter, drag coefficient, propellant mass fraction, exhaust velocity, initial inclination and propellant burning time. The program outputs are RLA's velocity and angle of inclination at the altitudes of 12 km, 16 km, and 20 km. Equations (2.1) – (2.3) are used to calculate the ascent trajectory of RLA. The Tsialkovski Equation (2.6) is used to calculate the rocket velocity change.

Equation (2.7) is used to calculate the drag loss. Equation (2.12) is used to calculate the gravity loss.

The aforementioned program **Rocket.m** performs calculations for the SSR. The user inputs SSR's mass, diameter, drag coefficient, propellant mass fraction, exhaust velocity, initial inclination and propellant burning time. The program calculates SSR's flight apogee height, flight apogee horizontal velocity, and flight apogee horizontal coordinate. It also calculates the rocket's range. SSR's height and velocity is recorded at every time interval dt during ascent. This data is used to calculate aerodynamic heating rates described below.

The program **Impact.m** performs calculations on the projectiles released at the apogee. The user inputs the projectile's mass, diameter, drag coefficient, apogee altitude, apogee, velocity, and apogee horizontal coordinate. The program calculates impact distance and velocity.

The programs **FirstStage.m**, **Rocket.m**, and **Impact.m** perform most of calculations used in this work. The results of these calculations are presented in Section 5.

2.2 Specific Impulse

In order to compare RLA to existing aircraft, we introduce some physical parameters of existing engines: Specific Impulse and thrust-to-weigh ratio. **Impulse** is the thrust integrated over time [34, p. 28]:

$$I = \int_0^{t_0} F(t)dt, \tag{2.13}$$

where t_0 is the engine working time and $F(t)$ is the engine thrust. **Specific Impulse** I_{sp} is impulse per unit mass of fuel consumed. It has the same units as velocity which is m/s. In some works, the specific impulse is divided by g and measured in seconds [34, p. 29]:

$$I_{sp} = \frac{v\ m/s}{9.81\ m/s^2} = \frac{v}{9.81}\ s. \tag{2.14}$$

In this work, we express the specific impulse in terms of velocity rather than time. For rocket engines, the specific impulse is the same as exhaust velocity. For jet engines, the specific impulse vastly exceeds the exhaust velocity. Typical specific impulse for a reusable rocket is 2,500 m/s. Typical specific impulse for a turbojet is 45,000 m/s, which is almost 20 times higher. The exhaust velocity of a jet engine is about 900 m/s, which is 50 times lower than the specific impulse.

A typical jet engine has a thrust-to-weigh ratio of 5:1 [34, p.3]. Jet engine thrust decreases with altitude at the same rate as the air density. A typical rocket engine has a thrust-to-weight ratio of 75:1 [34, p.3]. Rocket engine thrust increases very slightly with altitude.

Rocket aircraft have been used during WWII. These aircraft have not gained military or civilian use due to low impulse. RLA needs much lower impulse than other aircraft due to the short time per sortie.

3 Rockets to be Used in Both Stages

3.1 Solid Propellant Rocket

In the present and the two following sections we consider a solid propellant rocket. It is schematically presented in Figure 4 below.

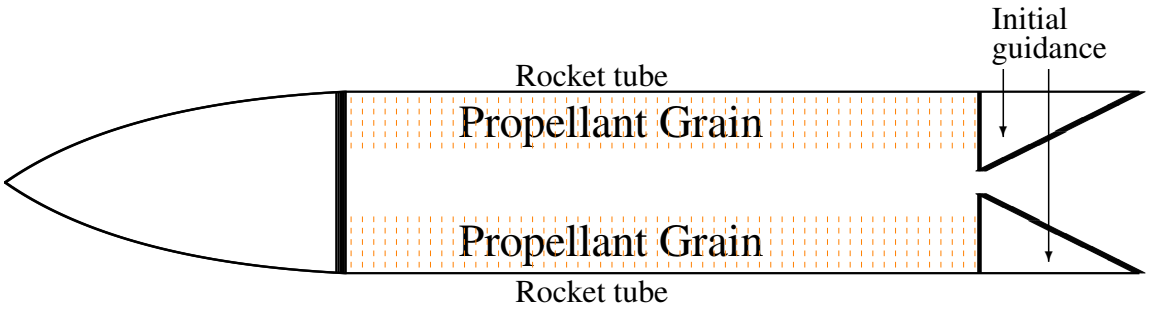

Figure 4: Solid propellant rocket

The RLA may use a solid propellant rocket for it's main engine. In that case, the engine and the propellant grain would take up at least 70% of RLA mass. The propellant grain would have to be reloaded into RLA for each sortie.

The SSR should consist of a one or more rocket with guided warheads. These rockets would be much less expensive than conventional rockets with similar range and payload. First, the fact that the SSR starts at an altitude of over 10 km with a velocity over 500 m/s would reduce $\triangle v$ needed for the rocket to achieve a given range by at least 750 m/s. Second, as we show in the following sections, a rocket starting at high altitude with high initial velocity does not need to experience high firing acceleration. While most artillery rockets burn their fuel within 2-3 seconds, the SSR will be able to achieve good result even if it takes 40-50 seconds to burn it's fuel. A solid-propellant rocket with slow burning fuel is much less expensive to manufacture. Third, slow-burning fuels have much lower flame temperature, which greatly reduces the cost of exhaust and initial guidance.

3.2 Propellant Composition

Most modern artillery rockets as well as space rocket boosters use a solid propellant containing 70% ammonium perchlorate (AP), 15% aluminum powder, and 15% HTPB binder [34, p.479]. Such propellant is expensive to manufacture due to the fact that AP is highly explosive. Other propellants contain high explosives and highly nitrated nitrocellulose. All of them are expensive and dangerous to handle. All the aforementioned propellants have flame temperatures of 2,500 ^oC to 3,500 ^oC.

SSR have a choice of fuels burning at lower temperature and rate. Some formulations contain ammonium nitrate (AN). The chemical formula for ammonium nitrate is NH_4NO_3. Its heat of formation is 367 kJ/mol. Ammonium Nitrate density is 1.725 g/cm^3 [35, p. 256]. Ammonium Nitrate undergoes phase transitions at -18 ^oC and +32 ^oC. These phase transitions are accompanied by volume change of about 4%, thus they must be avoided in order to avoid fuel grain destruction [35, p. 263]. Ammonium Nitrate can be phase-stabilized by addition of 10% potassium nitrate or

2% potassium fluoride [35, p. 267-268]. Other sources [36] claim that even 1% potassium fluoride is sufficient for phase stabilization.

Other formulations have mildly nitrated nitrocellulose. The chemical formula for Nitrocellulose is $C_6H_{10-x}O_5\left(NO_2\right)_x$. It's atomic mass is $162+45x$. Its binding energy is $\left(961.5-103.6\cdot x\right)kJ/mol$. The number $0<x<3$ determines the oxidizer content of nitrocellulose. Nitroglycerin (NG) is used in double base propellants with nitrocellulose [37]. Nitroglycerin formula is $H_5C_3N_3O_9$. Its atomic mass is 227 amu. Its heat of formation is 380 kJ/mol. The propellants we are interested in should have flame temperatures of 1,300 ^oC to 1,500 ^oC.

Below we list several propellants. In the first column, we list propellant composition. In the second column, we list the flame temperature. In the third column, we list exhaust velocity into vacuum given an initial pressure of 40 atm and expansion of 15. Both temperature and the exhaust velocity are calculated using the program called Rocket Propulsion Analsis [38], which is available online. The forth column lists the burning rate at 40 atm. The fifth column lists **power coefficient**. For almost all propellants, the burning rate is approximated by

$$r_b\left(P\right)=r_b\left(P_0\right)\left(\frac{P}{P_0}\right)^n, \tag{3.1}$$

where r_b is the burning rate, P is pressure, P_0 is the reference pressure, and n is the power coefficient.

Propellant Composition	Temperature at 40 atm	v_e at 40 atm, Exp 15 Vacuum	Burning rate	n coefficient at 40 atm
20% Binder, 72% AN, 8% MgAl [39]	1,280 ^oC	2,140 m/s	2.0 mm/s	0.5
20% Binder, 68% AN, 12% MgAl	1,450 ^oC	2,240 m/s	NA	NA
20% Binder, 64% AN, 16% MgAl [39]	1,700 ^oC	2,320 m/s	3.0 mm/s	0.5
25% Binder, 60% AN, 15% MgAl [39]	1,410 ^oC	2,170 m/s	1.6 mm/s	0.7
17.8% HTPB, 64% AN, 14.6% Mg, 3.6% AC [40]	1,660 ^oC	2,270 m/s	2.0 mm/s	0.05
Nitrocellulose 9% N	1,060 ^oC	1,990 m/s	NA	NA
Nitrocellulose 10% N	1,350 ^oC	2,090 m/s	NA	NA
Nitrocellulose 11% N	1,680 ^oC	2,200 m/s	NA	NA
Nitrocellulose 12% N	2,030 ^oC	2,290 m/s	NA	NA
Nitrocellulose 13% N	2,380 ^oC	2,420 m/s	NA	NA
Nitrocellulose 14% N	2,690 ^oC	2,530 m/s	NA	NA
90% Nitrocellulose 7.5% N, 10% Mg	1,290 ^oC	2,080 m/s	NA	NA
90% Nitrocellulose 8% N, 10% Mg	1,410 ^oC	2,130 m/s	NA	NA
90% Nitrocellulose 8.5% N, 10% Mg	1,540 ^oC	2,200 m/s	NA	NA
70% AP, 15% Al, 15% HTPB Standard Propellant [41]	2,880 ^oC	2,610 m/s	6.5 mm/s	0.35
56% NG, 44% Cellulose	1,340 ^oC	2,090 m/s	NA	NA
59% NG, 41% Cellulose	1,510 ^oC	2,150 m/s	NA	NA
66% NG, 34% Cellulose [42, p. 4-5]	1,950 ^oC	2,300 m/s	4.0 mm/s	0.7
77% NG, 23% Cellulose [42, p. 4-5]	2,560 ^oC	2,530 m/s	7.0 mm/s	0.7
82.5% NG, 17.5% Cellulose [42, p. 4-5]	2,790 ^oC	2,630 m/s	10 mm/s	0.7

Table 3: Performance of solid propellants (NA – not available)

The presence of magnesium greatly catalyses and helps the reaction to run to completion. Magnesium droplets combust very quickly and thus immediately add large amount of energy to the process. Magnesium has a melting point of 650 ^oC. Based on the data extrapolated from [43, p. 6-70], the boiling point of magnesium is 1,660 ^oC at 40 atm.

Finding a propellant optimal in terms of both cost and properties remains an open problem. For now we assume, that our propellant has flame temperature 1,450 ^oC, burning rate of 2.0 mm/s, and exhaust velocity of 2,100 m/s. Extrapolation of the data in [44, p.151] also predicts the aforementioned combination of burning rate and exhaust velocity. Using the densities of energetic materials in [44, p.37], the density of our propellant should be 1.6 g/cm^3.

3.3 Grain Shape

The grain shape is the shape of the fuel within the rocket tube. Different rockets use a wide variety of grain shapes illustrated in Figure 5 below [45]:

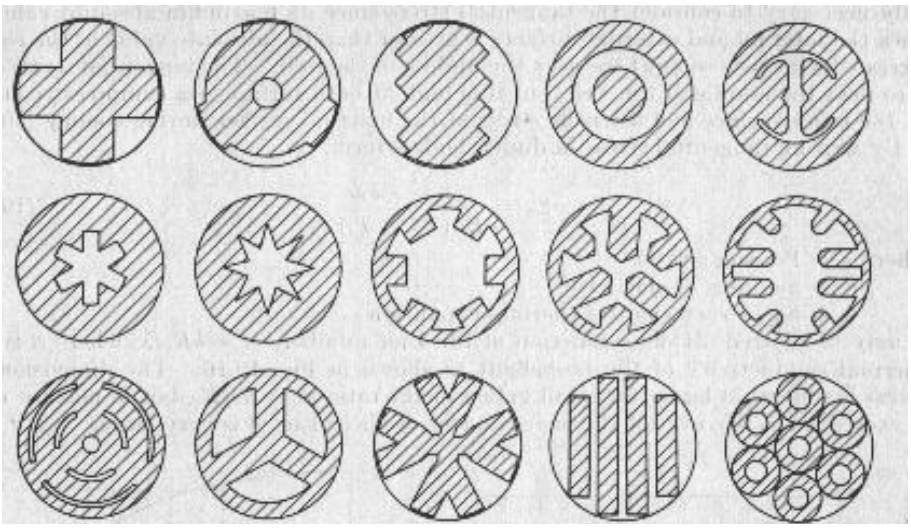

Figure 5: Propellant grain shapes

The shape may change over the length of the rocket tube. **Propellant loading** is the fraction of rocket tube volume occupied by the propellant. The best propellant grain shape for the SSR satisfies three requirements. First, the burning propellant surface area should experience minimal change as the propellant is burning. Second, the propellant loading should be as high as possible. Third, the design should be as simple as possible.

A diagram of a rocket motor cross-section is below:

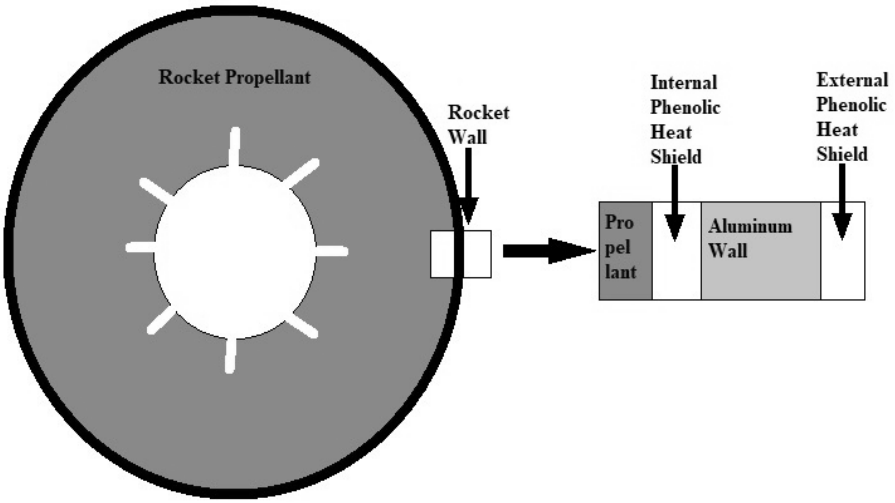

Figure 6: Rocket motor cross section

Aluminum 6061 T6 is one of the best candidates for the rocket wall. Aluminum 6061 T6 pipe of diameter up to 25 cm and wall thickness 1 cm is sold for \$14.30 per kg pipe weight [46]. It has density of 2.7 g/cm^3 and tensile yield strength of 2,720 atm [47]. The mass of solid propellant rocket wall for a given volume and pressure is inversely proportional to the wall's **specific strength**,

which is yield strength divided by density. Specific strength has units of

$$\frac{N/m^2}{kg/m^3} = \frac{N \cdot m}{kg} = \frac{J}{kg}. \tag{3.2}$$

Aluminum 6061 T6 has a specific strength of $1.15 \cdot 10^5\ J/kg$. Duralumin and titanium have specific strength about twice as high as Aluminum 6061 T6, but they are tens of times more expensive than Aluminum 6061 T6. Composite materials with **specific strength** of $1.7 \cdot 10^5\ J/kg$ and price of \$60 per kg in 2009 are available. These materials are widely used in compressed natural gas tanks [48]. Currently, these tanks are for sale at about \$60 per kg wall material. Unlike metals, composite materials experience almost no fatigue [49, p.18], which is important for reusable rocket engine of RLA. Cylinders made of composite materials almost never fail within 3,000 cycles of pressurization and depressurization [49, p.32].

3.4 Liquid Propellant Rocket

Large rockets use several oxidizers – liquid oxygen, concentrated solutions of hydrogen peroxide (H_2O_2) in water, nitric acid (HNO_3), nitrogen tetroxide (N_2O_4) [34, pp. 256-259]. An 95% solution of hydrogen peroxide can undergo catlytic decomposition producing steam and oxygen at 870 ^{o}C [38], which is above the autoignition temperature of most fueels. That is an important advantage for small rockets. In the past hydrogen peroxide had problems of instability, but with modern containers and stabilizers, concentrated hydrogen peroxide is very stable. In drum quantities, it loses up to 0.4% per year [50, p. 14]. Dissociation rate of hydrogen peroxide is inversely proportional to water content [51, p. 7] – thus high grade peroxide is more stable than low grade one.

Large rockets use several fuels – hydrocarbon fuels, hydrazine (N_2H_4), unsymmetrical dimethylhydrazine $\left((CH_3)_2NNH_2\right)$, monomethylhydrazine $\left((CH_3)NHNH_2\right)$, [34, pp. 259-26]. All forms of hydrazine are toxic and extremely expensive. Ethylene oxide has many advantages as a fuel for a small rocket, especially when the oxidizer is hydrogen peroxide. It decomposes rapidly and generates extra energy upon contact with hot steam and oxygen.

Performance of several liquid fuel-oxidizer combinations is tabulated in Table 4 below. In The first column, ethylene oxide is written as EthOx. The second column lists the oxidizer. HP95 denotes 95% solution of hydrogen peroxide. LO2 denotes liquid oxygen. The third column is the oxidiser to fuel mass ratio. The forth column is the temperature at rocket throat. The temperature of the flame where oxidizer and fuel contact is higher. The fifth column is exhaust velocity.

The values in the last three columns are deduced from the values calculated by Rocket Propulsion Analysis (RPA) program [38]. These values are actual rather than ideal. The ideal velocities are calculated by RPA. Actual sea level exhaust velocity is the ideal sea level exhaust velocity multiplied by 0.92. Actual vacuum exhaust velocity is the ideal vacuum exhaust velocity multiplied by 0.94.

Fuel	Oxidizer	Oxidizer to fuel ratio	Temperature	v_e at 40 atm, Expansion 15 Sea Level	v_e at 40 atm, Expansion 15 Vacuum
EthOx	HP95	1.0	1,464 ^{o}C	1,840 m/s	2,380 m/s
EthOx	HP95	3.8	2,654 ^{o}C	2,204 m/s	2,833 m/s
Methanol	HP95	1.35	1,463 ^{o}C	1,794 m/s	2,276 m/s
Methanol	HP95	3.3	2,407 ^{o}C	2,114 m/s	2,722 m/s
Propane	HP95	2.99	1,460 ^{o}C	1,869 m/s	2,370 m/s
Propane	HP95	7.8	2,561 ^{o}C	2,197 m/s	2,826 m/s
EthOx	LO2	0.44	1,470 ^{o}C	1,880 m/s	2,375 m/s
EthOx	LO2	0.52	1,800 ^{o}C	1,943 m/s	2,525 m/s
EthOx	LO2	1.8	3,300 ^{o}C	2,334 m/s	2,986 m/s
Methanol	LO2	0.59	1,480 ^{o}C	1,822 m/s	2,358 m/s
Methanol	LO2	0.68	1,790 ^{o}C	1,912 m/s	2,480 m/s
Methanol	LO2	1.5	2,960 ^{o}C	2,277 m/s	2,914 m/s
Propane	LO2	1.31	1,480 ^{o}C	1,958 m/s	2,529 m/s
Propane	LO2	1.45	1,800 ^{o}C	2,024 m/s	2,629 m/s
Propane	LO2	3.6	3,290 ^{o}C	2,388 m/s	3,055 m/s

Table 4: Performance of liquid bipropellants

As we have mentioned earlier, for a small rocket we would like a non-cryogenic oxidizer and exhaust temperature to be sustained at about 1,460 ^{o}C. At that temperature methanol fuel with 85% H_2O_2 oxidizer produces the lowest exhaust velocity, propane produces the highest, while ethylene oxide is the second best at 2,360 m/s. In our opinion, the advantages of ethylene oxide outweigh any disadvantages. For a large rocket the best fuel-oxidizer choice is propane and liquid oxygen at ratio 1.45.

Hypergolic propellants ignite as soon as propellant spray and fuel spray are combined. These propellants are especially useful for the non-returning SSR. Incorporating an expensive ignition system into SSR is an extra cost which is not returning. Most hypergolic propellants used in present rockets include hydrazine or one of it's derivatives, which are unreasonably expensive.

Red fuming nitric acid (RFNA) consists of 79% $HN0_3$ and 19% N_2O_4 [52, p. 165]. This oxidizer is hypergolic with fuel consisting of carene and norbornadiene. Concentrated hydrogen peroxide is hypergolic with the following fuel mixtures. First, it is hypergolic with ETA – the mixture of ethanolamine and 10% $CuCl_2$ [53, p.274]. Second, it is hypergolic with ETAFA – the mixture of 47.5% Ethanolamine, 47.5% Furfuryl Alcohol, and 5.0% $CuCl_2$ [54]. Third, it is hypergolic with pyrrole [55]. Forth, it is hypergolic with EEC – the mixture of 61% monoethanolamine, 30% ethanol, and 9% hydrated copper nitrate. On contact, EEC ignites with a delay of only $1.6 \cdot 10^{-2}$ s [56].

Performance of several hypergolic combinations is tabulated in Table 5 below. The second column lists the oxidizers. HP95 denotes 95% solution of hydrogen peroxide. The third column is the oxidiser to fuel mass ratio. The forth column is the temperature at rocket throat. The temperature of the flame where oxidizer and fuel contact is higher. The fifth column is exhaust

velocity.

Fuel	Oxidizer	Oxidizer to fuel ratio	Temperature	v_e at 40 atm, Expansion 15 Sea Level	v_e at 40 atm, Expansion 15 Vacuum
ETA	HP95	1.92	1,460 ^{o}C	1,723 m/s	2,186 m/s
ETA	HP95	3.4	2,220 ^{o}C	1,980 m/s	2,553 m/s
ETAFA	HP95	1.62	1,470 ^{o}C	1,708 m/s	2,211 m/s
ETAFA	HP95	3.8	2,408 ^{o}C	2,054 m/s	2,644 m/s
EEC	HP95	2.08	1,460 ^{o}C	1,780 m/s	2,257 m/s
EEC	HP95	4.6	2,367 ^{o}C	2,067 m/s	2,664 m/s

Table 5: Performance of hypergolic propellants

In Table 6 we tabulate the performance of several monopropellants. The second column is both the flame temperature and the exhaust temperature.

Monopropellant	Temperature	v_e at 40 atm, Expansion 15 Vacuum
60% Ethylene 40% N_2O	1,130 ^{o}C	2,055 m/s
50% Ethylene 50% N_2O	1,260 ^{o}C	2,150 m/s
40% Ethylene 60% N_2O	1,460 ^{o}C	2,270 m/s
11% Ethylene 89% N_2O	3,090 ^{o}C	2,790 m/s
Nitromethane	2,185 ^{o}C	2,570 m/s
80% Nitromethane 20% Methanol	1,270 ^{o}C	2,250 m/s
84.5% Nitromethane 15.5% Methanol	1,460 ^{o}C	2,315 m/s
54% Nitromethane 46% Nitroethane	1,460 ^{o}C	2,335 m/s

Table 6: Performance of liquid monopropellants

Monopropellants burning at 1,460 ^{o}C have slightly lower exhaust velocity than bipropellants – 2,270 m/s to 2,315 m/s. The choice of monopropellant or bipropellant would also depend on combustion process.

The first four rows of Table 6 represent Nitrous Oxide Fuel Blend. Scientists are working on stabilizing the formula containing 11% Ethylene 89% N_2O. In such proportions, the mixture is extremely reactive and very unstable. Mixtures with much lower concentrations of nitrous oxide are much more stable, have much lower combustion temperature, and thus have lower exhaust velocity. One advantage of nitrous oxide fuel mixture is that it has a low boiling point, thus it self-pressurises the fuel tank if it is kept at about 0 ^{o}C to 20 ^oC. Vapor pressure of nitrous oxide is tabulated below [57]:

Temperature	Vapour pressure	Liquid density
–23 ^{o}C	16.5 atm	1.04 kg/L
–12 ^{o}C	23.1 atm	0.98 kg/L
0 ^{o}C	31.3 atm	0.90 kg/L
10 ^{o}C	40.7 atm	0.84 kg/L
15 ^{o}C	45.1 atm	0.82 kg/L
21 ^{o}C	52.4 atm	0.75 kg/L

Table 7: Nitrous oxide properties

Now we access liquid propellant prices. The prices listed below are from 2010s, most commonly 2019. Furfuryl alcohol costs \$1.00 to \$2.00 per kg [58]. Ethanolamine costs about \$1.80 per kg [59]. Ethylene oxide costs \$1.50 per kg [60]. Ethylene costs \$0.90 per kg [61]. The 50% solution hydrogen peroxide in water costs \$0.50 per kg [62]. According to Indian data, 50% solution hydrogen peroxide in water costs \$0.40 per kg [63]. Given that hydrogen peroxide purification also requires processing work, 98% pure hydrogen peroxide should be more expensive than similar weight of hydrogen peroxide in 50% solution. Hydrogen Peroxide Handbook provides the latest data from 1967 [64]. At that time, hydrogen peroxide cost seven times as much as now if we adjust for inflation. An important point is that concentrating hydrogen peroxide from 70% to 98% increased it's price on peroxide basis only by 26%. Thus we can be certain that with prices for 50% solution and modern technology it is possible to produce 95% pure hydrogen peroxide at \$2.00 per kg. The prices of both the fuels and oxidizers are low enough to fuel the RLA.

As of 2019, Nitromethane in large quantities costs \$1,428 per 42 gallon drum or \$8 per kg [65]. One may worry that nitromethane prices will rise when the product is in greater demand, but it is unlikely. Nitromethane can be obtained by nitration of methane with nitric acid and oxygen at 435 ^{o}C. Nitration of ethane yields 10%-20% nitromethane and 80%-90% nitroethane [66, pp. 180 – 183]. Methane can be nitrated by nitric acid at 410 ^oC and 18:1 molar ratio of methane to nitric acid. The process is 33% efficient [67]. Nitrous Oxide costs \$8 – \$11 per kg [68]. The aforementioned prices can be considered low compared to the cost of the non-returning SSR.

4 The Rocket Launcher Aircraft

The role of RLA is to fire artillery rockets from high altitude at a considerable initial velocity. RLA should be able to perform the firing maneuver thousands of times during its' service. RLA is unmanned.

The RLA has to perform the following maneuvers (in the description below we suggest possible parameters of these maneuvers):

1. It is preferred, but not required that RLA should be a Vertical Takeoff Vertical Landing (VTVL) vehicle.

2. RLA must raise the SSR to a high **firing altitude** h_f, where the air resistance would have low effect on it. A reasonable altitude is $h_f \geq 10\ km$.

3. RLA must provide the artillery rocket with **initial velocity** $\mathbf{v}_0$ at release. The direction of $\mathbf{v}_0$ should be vertical or at an angle of up to 40^o to the vertical. The speed at release should be $v_0 \geq 500\ m/s$. The vertical component of the initial velocity should be $v_{0y} \geq 350\ m/s$.

4. Given that RLA releases the artillery rocket at an altitude h_f and vertical velocity v_{0y}, the ceiling of RLA should be
$$h_c = h_f + \frac{v_{0y}^2}{2g} \geq 20\ km. \tag{4.1}$$
During the sortie, RLA must avoid being hit by antiaircraft fire. As we discuss below, a RLA flying close to the firing site is much less vulnerable than a fighter or a bomber aircraft flying close to a target.

5. The RLA should complete each sortie in about 7 to 10 minutes. It should be able to be refuelled and reloaded with another set of artillery rockets as soon as possible. Under ideal conditions, RLA should be able to fly 5-6 sorties per hour and up to 90 sorties per day.

The RLA should have the main rocket engine and two or more auxiliary engines. The main rocket engine is used for the initial takeoff and acceleration. The auxiliary engines are used for cruising and landing. An diagram of RLA is presented in Figure 7 below.

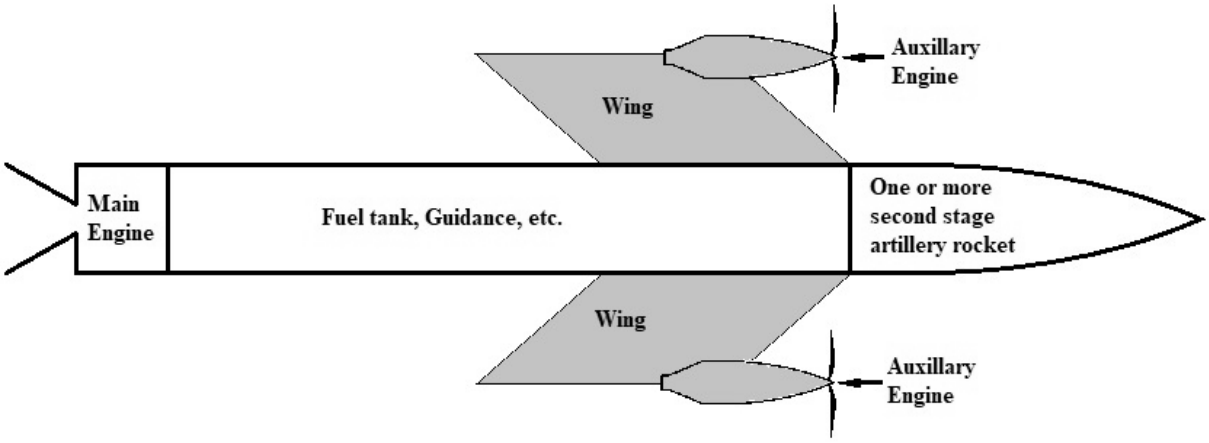

Figure 7: Rocket launcher aircraft

Below we list several concepts for auxiliary engines of RLA. Some of the concepts have been considered viable in 1940s and 1950s, but were abandoned due to their incompatibility with requirements for bomber and fighter aircraft. These concepts are air turborocket, rocketprop, and jet engine. These concepts are expounded in Subsections 5.2 – 5.4.

4.1 RLA Flight and Typical Schedule

A typical RLA sortie trajectory is shown in Figure 8 below. The first 2 minutes 22 seconds of flight are calculated by **FirstStage.m** program. The later times are estimated based on the RLA speed and distances involved.

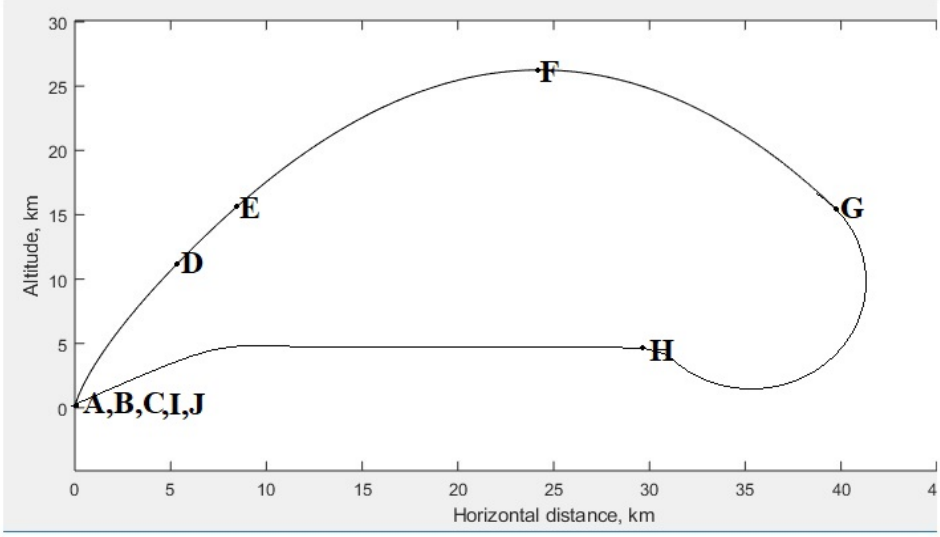

Figure 8: RLA sortie trajectory

The flight schedule for the sortie is presented below. It is given in minutes:seconds.

A 00:00 Main rocket engine starts.

B 00:05 Vertical liftoff using the main rocket engine.

C 00:08 Plane turns 5 ^{o} forward.

D 00:48 Main rocket engine off. Altitude 12 km. Speed 680 m/s.

E 00:56 Artillery rockets fired. Altitude 16 km. Speed 590 m/s.

F 01:41 Flight apogee. Altitude 26.3 km. Speed 335 m/s.

G 02:22 The maneuver of turning and gliding back begins. Auxiliary engines used. Altitude 15 km. Speed 542 m/s. Distance from base 40 km.

H 03:36 Turnaround maneuver completed. Auxiliary engines still on for flight to base. Altitude 5 km. Speed 200 m/s. Distance from base 29 km.

I 07:00 Flight to base completed. Auxiliary engines still on for vertical landing.

J 07:20 Vertical landing completed.

4.2 Rocketprop

A rocketprop combines a rocket and a propeller engine. Its rotary engine is similar to that of an air turborocket described in Fundamentals of Aircraft and Rocket Propulsion [69, p. 76]:

> (The propeller) is driven by a multi-stage turbine; the power to drive the turbine is derived from combustion of (rocket fuel) in a rocket-type combustion chamber. Since the gas temperature will be in the order of 3000 ^{o}C, additional fuel is sprayed into the combustion chamber for cooling purposes before the gas enters the turbine.

The turbine inlet temperature for a small uncooled turbine can be at most 800 ^{o}C [69, p.76]. The choice of fuel and propellant has to be such, that propellant excess would not produce carbon residue particles. After the gas leaves the turbine it further expands and comes out of the nozzle. Sometimes, before coming out of the nozzle, the gas is heated by an addition of extra oxidizer.

The turbine efficiency is at least 90% [69, p.430]. Turbine efficiency is not the measure of the total gas energy converted into motive power. Turbine efficiency is the fraction of the gas energy released under ideal expansion converted into motive power. The gas energy released under ideal expansion depends on initial gas temperature, initial gas pressure, final gas pressure, and chemical equilibrium composition of the gas. This energy can be calculated by the Rocket Propulsion Analysis program [38].

Performance for several propellants for aforementioned rotary engines is tabulated in Table 8 below. The first column is fuel. EthOx40 denotes 40% ethyl oxide and 60% water. EthOx50 denotes 50% ethyl oxide and 50% water. Ethanol50 denotes 50% ethanol in 50% water. The second column is oxidizer. LO2 denotes liquid oxygen. The fifth column is energy transmitted into engine rotary power per gram propellant, when the gas expands from 40 atm pressure to 3 atm pressure over a 90% efficient turbine. The sixth column is the exhaust velocity after the stream is further expanded from 3 atmospheres to 1 atmosphere.

Fuel	Oxidizer	Oxidizer to fuel ratio	Temperature	Propellant Energy	Exhaust Velocity
EthOx40	85% H_2O_2	0.6	810 ^{o}C	950 J/g	1,250 m/s
Methanol	85% H_2O_2	0.7	820 ^{o}C	1,070 J/g	1,170 m/s
Propane	65% H_2O_2	3.0	810 ^{o}C	1,070 J/g	1,180 m/s
Kerosine	65% H_2O_2	2.7	815 ^{o}C	1,020 J/g	1,150 m/s
EthOx50	LO2	0.2	810 ^{o}C	960 J/g	1,100 m/s
Methanol	LO2	0.28	810 ^{o}C	1,020 J/g	1,280 m/s
Ethanol50	LO2	0.38	810 ^{o}C	970 J/g	1,080 m/s

Table 8: Performance of propellants for turbine rotary engines

The propeller uses the mechanical power provided by the engine to create a backward airstream, and thus exert a force on the aircraft. Propeller efficiency is the fraction of rotary engine energy used to create the backward airstream and to propel the aircraft. The rest of the energy goes into creation of turbulence. The total efficiency of gearbox-propeller system is at least 70% [69, p. 583].

Propeller engine can be used up to Mach 0.7 [69, p. 119]. The rocketprop engine can be used along with the main rocket during the initial stages of acceleration of the RLA. It can also be used during the return of RLA to base and during landing. The rocketprop engine is much more suitable

for these purposes than a rocket, since at low velocity, the fuel produces much greater specific impulse.

Conventional turbojet, turboprop, and piston driven propeller engines provide much greater specific impulse than the rocketprop engine. The high specific impulse comes at a cost of much lower thrust-to-weight ratio. These engines are much more suitable for long range aircraft, while the rocketprop is much more suitable for the RLA.

4.3 Air Turborocket

Air turborocket is a modification of a rocketprop engine. Instead of a propeller, the turbine described in Section 4.2 drives an afterburning ducted fan. Air turborocket is shown in Figure 9 below:

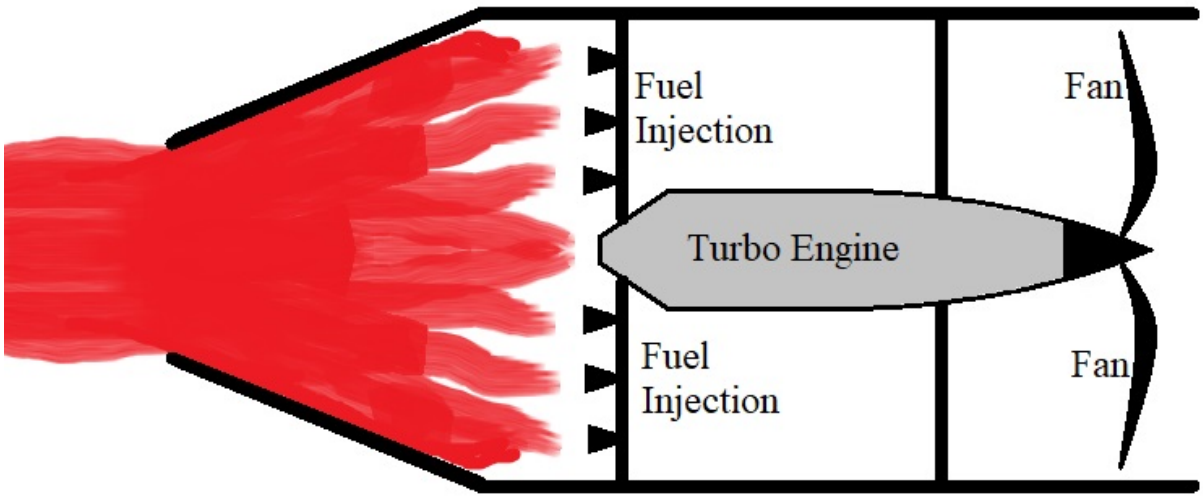

Figure 9: Air turborocket

Specific impulse of air turborocket built with relatively primitive technology available in 1955 is given in [70, p.43]. The turborocket uses gasoline fuel and nitric acid oxidizer. Specific impulse is tabulated in Table 9 below. The first column is the Mach number. The second column is the turbine compression ratio. Air already compressed by ram compression is further compressed by the turbine. The third column is the Specific Impulse.

Mach number	Fan compression ratio	Specific Impulse
0	2.1	7,340 m/s
0.5	2.1	6,400 m/s
1.0	1.9	6,450 m/s
1.5	1.8	6,220 m/s
2.0	1.7	7,900 m/s
2.3	1.6	8,500 m/s

Table 9: Performance of ATR for different Mach numbers

4.4 Turbojet Engine

Turbojet engines have been extensively developed for the last 80 years. They are widely used in aviation. They have excellent specific impulse in excess of 27,000 m/s, but their thrust-to-weight ratio is lower than that of air turborockets [70, p.45].

5 Rocket Performance

5.1 Performance of the Rocket Launcher Aircraft

In this subsection we calculate the **propellant mass fraction** f_p needed for RLA to fulfill **sortie requirements**. Sortie requirements consist of three components: RLA altitude at rocket release, RLA speed at rocket release, and the angle of RLA motion relative to the ground at rocket release. The **gross liftoff mass** M_{Tot} of RLA is the sum of the masses of four components: propellant used for liftoff and initial acceleration, SSR(s), fuel used by auxiliary engines during return and landing, and RLA itself. The **propellant mass fraction** f_p of RLA is the quotient of mass of propellant used for liftoff and initial acceleration to gross liftoff mass. The fuel used by auxiliary engines is not counted in f_p, since that fuel is used considerably after the main rocket stops working.

The propellant mass fraction is one of the most important parameters of RLA, since it determines the possible mass of the SSRs. The total distribution of mass in a fully loaded RLA can be written as

$$f_p + f_a + f_f + f_r = 1, \tag{5.1}$$

where f_p is the mass fraction of the propellant used by the main engine, f_a is the aircraft mass fraction or the ratio of empty weight to maximum takeoff weight, f_f is the mass fraction of fuel used by auxiliary engines, and f_r is the SSR mass fraction. In order to maximize the mass fraction of the SSRs, we must minimize the mass fraction of the three other components, but that runs into technical difficulties.

Mass fraction f_a can be estimated from similar aircraft. For F-16 Falcon fighter aircraft, the ratio of empty weight to maximum takeoff weight is $f_a = 0.45$ [71]. Mikoyan MiG-29K fighter aircraft also has $f_a = 0.45$ [72]. Mikoyan MiG-35 fighter aircraft has $f_a = 0.37$, but this aircraft is modern and expensive at unit price of $50 millon [73]. It should be possible to obtain smaller f_a, but that would either make RLA very fragile and vulnerable to any projectile fragment impact or very expensive or both. In this work, we use $f_a = 0.44$.

Mass fraction of fuel used by auxiliary engines should be about $f_f = .1$. The auxiliary engines have to provide power for RLA to cruise 40 km – 60 km to base and for aircraft landing. By the beginning of the return trip, RLA has burned the propellant for the main engine and released the SSR. RLA begins the return trip at about half the liftoff mass. If the auxiliary engines are rocketprop or air turborocket, then f_f is higher while f_a is lower. If the auxiliary engines are turboprop or turbojet, then f_f is lower while f_a is higher. Overall, the sum of aircraft mass fraction

and auxiliary fuel mass fraction should be

$$f_a + f_f \approx 0.54. \tag{5.2}$$

Substituting (5.2) into (5.1), we obtain

$$f_p + f_r = 0.46. \tag{5.3}$$

Below we describe the results of a simulation determining f_p based on sortie requirements. As mentioned in Subsection 2.1, the MatLab program **FirstStage.m** takes in several coefficients including propellant mass fraction f_p and calculates the rocket velocity at altitudes of 12 km, 16 km, and 20 km. Using this program we are able to find the right f_p given the resulting velocity and altitude of RLA.

RLA is shown in Fig. 7. The main body has a diameter of 1.25 m, length of 7.5 m. The gross liftoff mass is $M_{\text{Tot}} = 10,000\ kg$. The exhaust velocity of the main rocket engine is $v_e = 2,450\ m/s$. As we have demonstrated in Subsection 3.4, it is possible to increase exhaust velocity of the main engine to $v_e = 3,000\ m/s$ if we use oxidiser to fuel ratio which produces combustion temperature over 3,000 ^{o}C. In that case, the rocket engine would no longer be reusable.

Using RASAero software [74] we have calculated the drag coefficient for aforementioned artillery rocket at different Mach numbers and presented in Table 10 below.

$\mathscr{M}$	.25	.50	.75	.90	1.05	1.25	1.50	1.75	2.00
C_d	.18	.18	.17	.17	.73	.57	.50	.45	.42
$\mathscr{M}$	2.25	2.50	3.00	3.50	4.00	4.50	5.00	5.50	6.00
C_d	.40	.38	.35	.32	.30	.29	.27	.27	.26

Table 10: Drag coefficient RLA

Using a MatLab program **FirstStage.m** described in Subsection 2.1, we have calculated propellant mass fraction and several other flight parameters for different sortie requirements. The results are below:

1. **Sortie A**: RLA altitude at rocket release: 12 km. RLA speed at rocket release: 500 m/s. Angle of RLA motion relative to the ground at rocket release: 68^o.
   Propellant fraction: $p_f = 0.334$.
   Secondary rocket mass fraction: $p_r = 0.126$.
   Rocket engine firing time: 40 s. Rockets fired at: 42.9 s. Rocket Velocity Gain: 966 m/s. Drag loss: 69 m/s. Gravity loss: 229 m/s. Thrust to weight ratio: 2.03.

2. **Sortie B**: RLA altitude at rocket release: 16 km. RLA speed at rocket release: 600 m/s. Angle of RLA motion relative to the ground at rocket release: 65^o.
   Propellant fraction: $p_f = 0.379$.
   Secondary rocket mass fraction: $p_r = 0.081$.
   Rocket engine firing time: 40 s. Rockets fired at: 45.4 s. Rocket Velocity Gain: 1,138 m/s. Drag loss: 114 m/s. Gravity loss: 231 m/s. Thrust to weight ratio: 2.32.

3. **Sortie C**: RLA altitude at rocket release: 20 km. RLA speed at rocket release: 700 m/s. Angle of RLA motion relative to the ground at rocket release: 62^o.
   Propellant fraction: $p_f = 0.417$.
   Secondary rocket mass fraction: $p_r = 0.043$.
   Rocket engine firing time: 40 s. Rockets fired at: 48 s. Rocket Velocity Gain: 1293 m/s. Drag loss: 148 m/s. Gravity loss: 234 m/s. Thrust to weight ratio: 2.56.

For Sortie C, the secondary rocket mass fraction is very low, thus some engineering work must be required to fire rockets from 20 km altitude. The aircraft's mass fraction can be slightly reduced by the use of hardier materials. The exhaust velocity can be slightly increased within the confines of engine reusability. External disposable propellant tanks may be used.

5.2 Performance of 30 cm Second Stage Rocket (SSR)

The rocket is shown below:

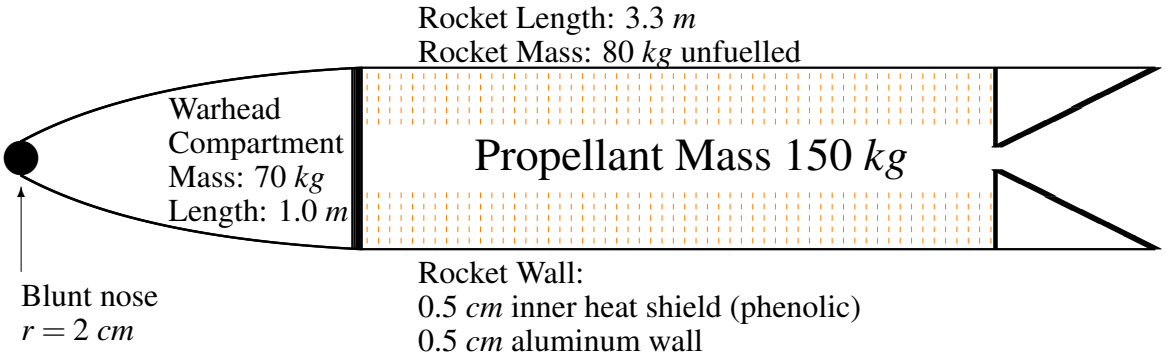

Figure 10: Second stage rocket

The rocket has diameter of 30 cm, total mass of 300 kg, total length of 4.3 m of which 1.0 m is the ogive warhead compartment. The propellant mass fraction is $f_p = 0.50$. The exhaust velocity is $v_e = 2,100\ m/s$.

Using RASAero software [74] we have calculated the drag coefficient for aforementioned artillery rocket at different Mach numbers and presented in Table 11 below. The RASAero software takes in rocket radius, rocket cylinder length, rocket nose length, and rocket nose shape. The software calculates the drag coefficient.

$\mathscr{M}$	.25	.50	.75	1.00	1.25	1.50	1.75	2.00	2.25	2.50	2.75	3.00
C_d	.265	.260	.261	.380	.432	.404	.381	.352	.328	.308	.289	.273
$\mathscr{M}$	3.25	3.50	3.75	4.00	4.25	4.50	4.75	5.00	5.25	5.50	5.75	6.00
C_d	.259	.246	.235	.225	.216	.208	.200	.193	.187	.181	.175	.168
$\mathscr{M}$	6.25	6.50	6.75	7.00	7.25	7.50	7.75	8.00	8.25	8.50	8.75	9.00
C_d	.163	.159	.154	.150	.147	.144	.141	.139	.137	.135	.133	.131

Table 11: Drag coefficient for 30 cm rocket

The warhead compartment consists of a 10 kg container which ejects up to 60 kg of projectiles at the apogee. The projectiles are guided. They are made of high density material like tungsten or depleted uranium.

Performance of SSR for several release altitudes, release velocities, and firing times is tabulated below:

Release altitude: 12 km. Release velocity: 500 m/s.					
Firing time, s	30	40	50	60	80
Optimal firing angle, ^{o}	54	57	61	64	68
Flight time, s	282	288	289	289	277
Drag loss, m/s	98	84	76	69	62
Gravity loss, m/s	93	131	169	209	285
Rocket Velocity Gain, m/s	1457	1457	1457	1456	1459
Flight apogee, km	93	94	92	89	77
Range, km	327	317	304	291	263
Release altitude: 16 km. Release velocity: 600 m/s.					
Firing time, s	30	40	50	60	80
Optimal firing angle, ^{o}	54	57	59	60	65
Flight time, s	311	314	311	303	300
Drag loss, m/s	51	45	42	40	35
Gravity loss, m/s	90	124	158	188	263
Rocket Velocity Gain, m/s	1457	1457	1457	1456	1456
Flight apogee, km	116	115	110	102	95
Range, km	386	373	361	349	318
Release altitude: 20 km. Release velocity: 700 m/s.					
Firing time, s	30	40	50	60	80
Optimal firing angle, ^{o}	53	54	56	58	62
Flight time, s	320	325	323	322	318
Drag loss, m/s	29	26	24	22	20
Gravity loss, m/s	82	113	144	176	242
Rocket Velocity Gain, m/s	1457	1457	1457	1456	1459
Flight apogee, km	125	126	122	118	111
Range, km	444	431	417	403	374

Table 12: Performance of 30 cm rocket

5.3 Impact Velocity Calculation

5.3.1 Hypervelocity Projectile

In this subsection we calculate the impact velocity for the warhead consisting of the Hypervelocity Projectile (HPV). HPV is described in Subsection 1.2 and presented in Fig. 3. Recall, that HPV's weight is 11.4 kg, length 64.2 cm, and caliber 7.83 cm. A 70 kg warhead compartment can carry up to 5 such projectiles.

Using RASAero software [74] we have calculated the drag coefficient for the HPV at different Mach numbers and presented in Table 13 below. As we mentioned earlier, the RASAero software takes in rocket radius, rocket cylinder length, rocket nose length, and rocket nose shape. The software calculates the drag coefficient.

$\mathscr{M}$	.25	.50	.75	1.00	1.25	1.50	1.75	2.00	2.25	2.50	2.75
C_d	.208	.203	.202	.289	.336	.325	.292	.265	.243	.225	.208
$\mathscr{M}$	3.00	3.25	3.50	3.75	4.00	4.25	4.50	4.75	5.00	5.25	5.50
C_d	.194	.181	.171	.161	.152	.145	.139	.133	.127	.122	.117
$\mathscr{M}$	5.75	6.00	6.25	6.50	6.75	7.00	7.25	7.50	7.75	8.00	
C_d	.112	.106	.103	.099	.095	.091	.089	.087	.085	.083	

Table 13: Drag coefficient for HPV projectile

In **FirstStage.m** and **Rocket.m** simulations described in Subsection 6.2, we have calculated SSR apogee altitude, SSR apogee velocity, and SSR apogee horizontal distance. These calculations were performed for release altitudes of 12 km, 16 km, and 20 km. Corresponding release velocities were 500 m/s, 600 m/s, and 700 m/s. We input the results of **FirstStage.m** and **Rocket.m** simulations and the drag coefficient tabulated in Table 13 above into Impact.m. The program **Impact.m** calculates the projectiles' ranges, impact velocities, and descent drag loss.

Stage 2 rocket initial velocity, m/s	500	600	700
Stage 2 rocket firing altitude, km	12	16	20
Stage 2 rocket firing time, s	80	80	80
Flight apogee, km	76.8	95.4	110.6
Apogee velocity, m/s	1,150	1,241	1,349
Range, km	263.7	319	373.7
Impact velocity, m/s	1,111	1,268	1,414
Descent drag loss, m/s	572	579	583

Table 14: HPV warhead performance

As we see from the above table, the HPV has very high aerodynamic drag loss. Even though minimization of drag loss has been an important goal in the design of HPV, the main design goal for HPV was an ability to survive the acceleration of a cannon launch. Rocket launched projectiles do not require the ability to survive extreme acceleration, hence HPV design may be suboptimal for rocket-launched projectiles.

5.3.2 European Hypersonic Projectile

The Europrojectile has not been built yet and exists only as a concept. Based on paper [75], we present a sketch below.

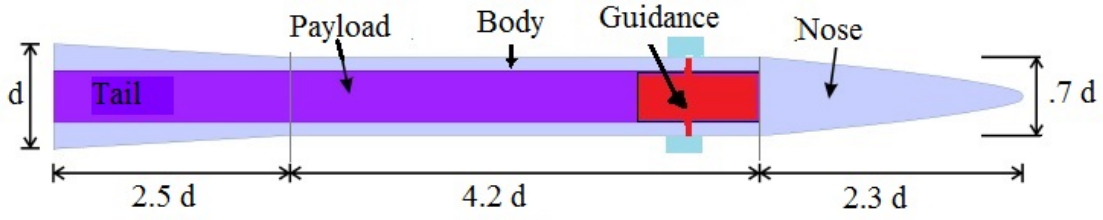

Figure 11: Europrojectile

In the above figure, d is the base diameter. We will consider several diameters. The length of the projectile is 9 d. The tail of the projectile is a conical frustum with height 2.5 d and radii 0.5 d and 0.35 d. The volume of the tail is

$$\frac{\pi}{3}H\left(R_1^2+R_1R_2+R_2^2\right)=\frac{\pi}{3}2.5d\left(.5^2d^2+.5\cdot.35d^2+.35^2d^2\right)=1.43d^3. \tag{5.4}$$

The volume of the cylindrical body of height 4.2 d and radius 0.35 d is

$$\pi HR^2=\frac{\pi}{4}(4.2d)(.7d)^2=1.62d^3. \tag{5.5}$$

The volume for LV–Haack nose is derived from the cone equations [76] as $0.56\pi LR^2$, where L is the cone length and R is the cone radius. Thus, in our case the cone volume is $0.50d^3$. The total volume of the projectile is $3.55d^3$. If the average density of the projectile is ρ, then its total mass is

$$M_p=3.55d^3\rho. \tag{5.6}$$

The projectile of our choice has caliber $d=7.5$ cm, density $\rho=11$ g/cm^3, length 67.5 cm, and weight of 16.5 kg. A 70 kg warhead compartment can carry up to 3 such projectiles. Using RASAero software [74] we have calculated the drag coefficient for the HPV at different Mach numbers and presented in Table 15 below.

M	.25	.50	.75	1.00	1.25	1.50	1.75	2.00	2.25	2.50	2.75
C_d	.184	.182	.181	.264	.297	.268	.242	.219	.200	.184	.169
M	3.00	3.25	3.50	3.75	4.00	4.25	4.50	4.75	5.00	5.25	5.50
C_d	.156	.145	.135	.126	.119	.112	.106	.100	.095	.091	.086
M	5.75	6.00	6.25	6.50	6.75	7.00	7.25	7.05	7.75	8.00	
C_d	.081	.076	.072	.069	.066	.062	.060	.058	.056	.055	

Table 15: Drag coefficient for Europrojectile

Using the drag coefficient presented above along with data calculated in the Subsection 5.2, we have calculated the impact velocity and Drag loss of Europrojectile.

Stage 2 rocket initial velocity, m/s	500	600	700
Stage 2 rocket firing altitude, km	12	16	20
Stage 2 rocket firing time, s	80	80	80
Flight apogee, km	76.8	95.4	110.6
Apogee velocity, m/s	1,150	1,241	1,349
Range, km	264	319	373.9
Impact velocity, m/s	1,399	1,573	1,735
Descent drag loss, m/s	284	274	273

Table 16: Europrojectile warhead performance

From the above table we see that the Europrojectile has high impact velocity. At such velocity, the projectile can inflict considerable damage due to kinetic energy. One type of kinetic energy projectile which inflicts high area damage is a flechette projectile [77, p.61]. This projectile explodes at a distance of about a hundred meters from the target releasing thousands of tungsten flechettes weighing 1 g to 2 g. For a projectile with high impact velocity, the flechettes cause extensive damage.

6 Aerodynamic Heating and Thermal Protection

An object moving through atmosphere or any gas at supersonic velocity experiences two types of aerodynamic heating. The first type is shock wave heating. The supersonic object produces a shock wave in front of it. Air/gas temperature behind a shock wave can be very high – up to 20,000 ^oC [78, p. p.9]. For the rockets we are considering the temperature of the shocked air will never exceed “mere" 1,850 ^oC, but this temperature is still high.

The second type is skin friction heating. This is due to the high-speed friction of the rocket nose and sides against supersonic or hypersonic stream. Generally, this friction contributes more to overall dynamic heating than the shock wave.

In this work, we use simplified expressions to find an upper bound of heat flux. Exact calculation of heat flux requires extensive calculations using Aerodynamic Theory. Designing an actual thermal protection requires not only advanced theoretical and computational work, but also many laboratory experiments.

The expressions themselves do not differentiate between heat flux caused by the shock wave and heat flux caused by friction. The heat transfer equations fall into two different classes. These classes represent two types of flow – laminar and turbulent. In this Section we present the expressions for heat flux generated by laminar and turbulent flows.

At the nose of the vehicle, the flow is always laminar. At a short distance from the nose, it becomes turbulent and stays turbulent for the rest of the vehicle length. Generally, turbulent flow transfers a higher heat flux to the wall then a laminar flow.

The expressions used to estimate laminar and turbulent heat fluxes on different types of surfaces have been obtained over decades as mathematical fits to experimental data. These expressions may or may not have deeper physical meanings. Some data patterns may have more than one expression providing a good fit.

One of the main advantages our RLA – SSR system has over conventional long-range ballistic missiles is the relatively low heating of SSR during ascent. The SSR reaches high velocities only in significantly rarified atmosphere. Thus, the heat flux and heat load are considerably lower than those experienced by a conventional long-range rocket.

6.1 General Expressions for Heat Flux

As a rocket flies through the air at high speed, it experiences aerodynamic heating. The nose facing the air flow and the nose cone experience heating due to the air compression shock wave. Any surface inclined at a small angle or parallel to the flow experiences heating due to the skin friction. The rocket nose experiences laminar flow heating, while the nose cone and rocket cylinder experience turbulent flow heating. Even though some parts of the nose cone may experience laminar flow at high altitudes, turbulent flow heating rate still provides a valid upper bound. In this Subsection we present general expressions for the heat flux experienced by different points on a rocket surface during ascent and reentry.

Recovery temperature is the temperature the surface would have if it lost zero energy by thermal radiation or inward conduction. Recovery temperature is such that air at that temperature has enthalpy h_{aw}. Adiabatic wall enthalpy, h_{aw} is given by

$$h_{aw} = h_a + r_f \frac{v^2}{2}. \tag{6.1}$$

where h_a is the ambient air enthalpy, v is the vehicle velocity, and r_f is the **recovery factor** [81, p.9]. The recovery factor is a dimensionless number, which is 1 at a stagnation point, and 0.9 for a turbulent boundary flow [79, p.100]. A crude approximation for the recovery temperature is given by [79, p.100]:

$$T_r = T_a \left(1 + .2 r_f \mathscr{M}^2\right), \tag{6.2}$$

where T_r is the recovery temperature, T_a is the ambient air temperature.

6.1.1 Stagnation Point Heat Flux

The stagnation point is a point in a flow field where the local velocity of the fluid is zero [80, p.17]. The nose tip is the only stagnation point in the flow around a rocket. The laminar heat flux to the stagnation point can be approximated by [81, p.6, Eq. (40)]:

$$\dot{Q}_S^{\text{laminar}} = 7,190 \frac{W}{m^2} \sqrt{\frac{\rho}{r}} \mathscr{M}^3 \frac{h_{aw} - h_w}{h_{aw} - h_a}, \tag{6.3}$$

where ρ is the air density measured in kg/m^3, r is the nose radius in meters, h_w is the specific enthalpy of the air at the wall, h_{aw} is the specific enthalpy of the air at a hypothetical adiabatic wall, h_a is the specific enthalpy of the ambient air. Q_S denotes the total thermal energy absorbed by the stagnation point, and $\dot{Q}_S$ is it's time derivative. For a typical sound velocity of 340 m/s, (6.3) can

be written as:

$$\dot{Q}_S^{\text{laminar}} = \dot{Q}_K \sqrt{\frac{\rho}{r}} v^3 \frac{h_{aw} - h_w}{h_{aw} - h_a}, \tag{6.4}$$

where v is the rocket velocity in m/s with respect to air and

$$\dot{Q}_K = 1.83 \cdot 10^{-4} \frac{W}{m^2} \tag{6.5}$$

is a constant. Sutton and Graves give a similar expression [82] with

$$\dot{Q}_K = 1.74 \cdot 10^{-4} \frac{W}{m^2} \tag{6.6}$$

According to Chapman [83],

$$\dot{Q}_K = 1.63 \cdot 10^{-4} \frac{W}{m^2} \tag{6.7}$$

Detra and Hidalgo give a velocity dependent expression [84],

$$\dot{Q}_K = 1.45 \cdot 10^{-4} \frac{W}{m^2} V_{\text{kps}}^{0.15}, \tag{6.8}$$

where V_{kps} is the rocket velocity in kilometers per second. In this work, we use $\dot{Q}_K = 1.83 \cdot 10^{-4}\ W/m^2$, which is the highest heating rate.

In a feasibility study, an estimate accurate to 20% is more than sufficient. In an actual design, the heat flux at every point and under a wide range of conditions will have to be calculated with a great accuracy.

According to [85], a crude approximation for (6.4) is

$$\dot{Q}_S^{\text{laminar}} = \dot{Q}_K \sqrt{\frac{\rho}{r}} v^3 \frac{h_{aw} - h_w}{h_{aw} - h_a} = \dot{Q}_K \sqrt{\frac{\rho}{r}} v^3 \frac{T_r - T_w}{T_r - T_a}, \tag{6.9}$$

where T_w is the rocket wall temperature, T_a is the temperature of surrounding air, and T_r is the recovery temperature. By including the blackbody radiation emanating from the rocket, we obtain the total heat flux passing through the stagnation point:

$$\dot{Q}_S^{\text{laminar}} = \dot{Q}_K \sqrt{\frac{\rho}{r}} v^3 \frac{h_{aw} - h_w}{h_{aw} - h_a} - e_w \sigma_B T_w^4, \tag{6.10}$$

where $\sigma_B = 5.67 \cdot 10^{-8}\ W/m^2K^4$ is the Stefan–Boltzmann constant, and $e_w < 1$ is the wall emissivity.

6.1.2 General Turbulent Flow Heat Flux

Turbulent flow heat flux is generally 3 to 6 times greater than laminar flow heat flux. The hypersonic flow around any rocket almost always starts out laminar and then turns turbulent. The transition from laminar to turbulent flow occurs at Reynolds number $10^5 \leq Re \leq 10^6$ [93, p.19].

The Reynolds number is defined in Equations (6.14) and (6.16) below. The flow is turbulent over almost all surface area of the hypersonic vehicles we are considering in this book.

A wall parallel to the air stream and having the same temperature as the air behind the shock wave experiences the following heat flux:

$$\dot{Q}^{\text{turbulent}} = 20,900\ \frac{W}{m^2}\ \rho^{.8} \mathscr{M}^{2.8} (ry)^{-.2}\ \frac{h_{aw} - h_w}{h_{aw} - h_a} = 1.71 \cdot 10^{-3}\ \frac{W}{m^2}\ \rho^{.8} v^{2.8} (ry)^{-.2}\ \frac{h_{aw} - h_w}{h_{aw} - h_a}, \tag{6.11}$$

where $\mathscr{M}$ is the Mach number, v is the rocket velocity in m/s, ρ is air density in kg/m^3 and ry is the distance from the stagnation point in m [79, p.100].

Below we estimate the skin friction heat flux for general wall temperature and inclination. According to [81, p.iii], the skin friction heat transfer is defined in terms of Stanton number,

$$\dot{Q}^{\text{turbulent}} = St \cdot \rho\ v \left(h_{aw} - h_w\right) = St \cdot \rho\ v \left(h_{aw} - h_a\right) \frac{h_{aw} - h_w}{h_{aw} - h_a}. \tag{6.12}$$

The enthalpy supplied to the air by the shock wave travelling in front of the moving rocket is equal to $v^2/2$. Thus,

$$h_{aw} - h_a = \frac{v^2}{2}. \tag{6.13}$$

Substituting (6.13) into (6.12), we obtain

$$\dot{Q}^{\text{turbulent}} = St \cdot \rho\ v \left(h_{aw} - h_a\right) \frac{h_{aw} - h_w}{h_{aw} - h_a} = St\ \frac{\rho\ v^3}{2}\ \frac{h_{aw} - h_w}{h_{aw} - h_a}. \tag{6.14}$$

The Stanton number at distance ry from the leading edge can be expressed in terms of skin friction coefficient [89, p.305]:

$$St(ry) = \frac{C_f(ry)/2}{1 + 13\left(Pr^{2/3} - 1\right)\sqrt{C_f(ry)/2}}, \tag{6.15}$$

where $C_f(ry)$ is the skin friction coefficient at distance ry from the leading edge and Pr is the Prandtl number. The Prandtl number for air is at least 0.71. The skin friction coefficient never exceeds 0.008. Substituting these values into (6.15) we obtain

$$St(ry) \leq 0.60\ C_f(ry). \tag{6.16}$$

Substituting (6.16) into (6.14), we obtain

$$\dot{Q}^{\text{turbulent}} = 0.30\ C_f(ry)\ \rho\ v^3. \tag{6.17}$$

In order to calculate the skin friction coefficient, we introduce the **Reynolds number**. The

Reynolds number for a point on a rocket body is given by [91, p.6]

$$Re = \frac{\rho v x}{\mu}, \tag{6.18}$$

where x is the distance of a point from the stagnation point or the leading edge.The dynamic viscosity of the air is [90, p.20-21]:

$$\mu \lessapprox 1.7 \cdot 10^{-5} \frac{kg}{m\ s} \left(\frac{T}{240\ ^o K} \right)^{0.7}. \tag{6.19}$$

The temperature of 240 ^{o}K is close to the ambient air temperature in the region where all maneuvers described in this work are performed. Combining (6.18) and (6.19), we obtain the Reynolds number for any point on the rocket surface:

$$Re \approx 70 \cdot 10^6 \left(\frac{\rho}{1\ kg/m^3} \right) \left(\frac{v}{1\ km/s} \right) \left(\frac{x}{1\ m} \right). \tag{6.20}$$

The above equation is valid for ambient air temperature for most maneuvers. The effect of heating of air by friction and shock wave is described below.

The skin friction coefficient is very well approximated by [92, p.4]:

$$C_f = 0.295 \frac{T_a}{T^*} \left[\log \left(Re \frac{T_a}{T^*} \frac{\mu_a}{\mu^*} \right) \right]^{-2.45}, \tag{6.21}$$

where T_a is the general air temperature, T^* is the air temperature at the boundary, μ_a is the general air viscosity, and T^* is the viscosity at the boundary. Expression (6.21) shows excellent agreement with experiment [92, p.8]. The temperature at the boundary is the temperature corresponding to the enthalpy h^*, which is [91, p.6]:

$$h^* = 0.22\ h_{aw} + 0.50\ h_w + 0.28\ h_a, \tag{6.22}$$

where h_{aw} is the adiabatic enthalpy, h_w is the enthalpy of air at wall temperature, and h_a is the enthalpy of ambient air. The term T_a/T^* in Eq. (6.21) is due to the fact that the air density is inversely proportional to the air temperature, and the friction force is directly proportional to the air density.

From (6.19), air viscosity grows approximately as temperature to the power 0.7. Thus,

$$\begin{aligned} C_f &= 0.295 \frac{T_a}{T^*} \left[\log \left(Re \frac{T_a}{T^*} \frac{\mu_a}{\mu^*} \right) \right]^{-2.45} \leq 0.295 \frac{T_a}{T^*} \left[\log \left(Re \left(\frac{T_a}{T^*} \right)^{1.7} \right) \right]^{-2.45} \\ &= 0.295 \frac{T_a}{T^*} \left[\log Re + 1.7 \log \left(\frac{T_a}{T^*} \right) \right]^{-2.45} = \frac{0.295\ \left[\log Re - 1.7 \log \left(T^*/T_a \right) \right]^{-2.45}}{T^*/T_a}. \end{aligned} \tag{6.23}$$

In Equation (6.23) above, log represents log base 10. We express (6.23) in terms of natural loga-

rithm:

$$C_f = \frac{2.28\ [\ln Re - 1.7 \ln (T^*/T_a)]^{-2.45}}{T^*/T_a}. \tag{6.24}$$

Combining (6.24) and (6.17), we obtain

$$\dot{Q}^{\text{turbulent}} = \frac{0.68\ [\ln Re - 1.7 \ln (T^*/T_a)]^{-2.45}}{T^*/T_a}\ \rho\ v^3\ \frac{h_{aw} - h_w}{h_{aw} - h_a}. \tag{6.25}$$

For the rockets and velocities we are considering, the Reynolds number varies between $1 \cdot 10^6$ and $1 \cdot 10^8$. The quotient T^*/T_a varies between 1 and 8. For all values of Re and T^*/T_a considered, C_f is strongly and strictly decreasing function of T^*/T_a. Hence, skin friction coefficient and turbulent heating are strongly decreasing with rising wall temperature.

6.1.3 Rocket Cylinder

For the rocket cylinder of SSR, the turbulent flow heat flux is calculated by (6.25) with the Reynolds number Re given by (6.20). At the base of the rocket cylinder, the distance from the stagnation point is $x = 1\ m$. Substituting this distance into (6.20), we obtain the Reynolds number for the leading edge:

$$Re \approx 70 \cdot 10^6 \left(\frac{\rho}{1\ kg/m^3}\right) \left(\frac{v}{1\ km/s}\right). \tag{6.26}$$

For further parts of the rocket cylinder, the Reynolds number is higher and the heat flux is a little lower.

6.1.4 Nose Cone

Turbulent flow heating rate for a cone is about 1.3 times greater than that for a plane [94, p. 11]. Another factor leading to an increase in turbulent flow heating rate on a cone relative to cylinder wall is the fact that the air pressure on the cone will exceed atmospheric pressure by a factor of

$$\frac{P_w}{P} = 1 + \frac{\gamma}{2}\ \mathscr{M}^2\ \left(\sin\theta\right)^2 \leq 1 + 6 \cdot 10^{-6}\ \left(\sin\theta\right)^2 v^2, \tag{6.27}$$

where $\mathscr{M}$ is the Mach number and v is the rocket velocity in m/s, and θ is the angle between the cone surface and the oncoming air stream. The heat transfer rate given in (6.25) will be multiplied by the same amount. Thus,

$$\begin{aligned} \dot{Q}_{\text{cone}}^{\text{turbulent}} &\leq \left(1 + 6 \cdot 10^{-6}\ \left(\sin\theta\right)^2 v^2\right) \\ &\times \frac{0.88\ [\ln Re - 1.7 \ln (T^*/T_a)]^{-2.45}}{T^*/T_a}\ \rho\ v^3\ \frac{h_{aw} - h_w}{h_{aw} - h_a}, \end{aligned} \tag{6.28}$$

where T^* is the temperature for which air enthalpy is given by (6.22), T_a is the air temperature, T_w is the rocket wall temperature, and Re is the Reynolds number given by (6.20).

Using the above information about the aerodynamic heating we have written a MatLab program **ThermalAnalysis.m**. This program calculates the temperatures of SSR stagnation point, several points on SSR nose cone, and rocket cylinder base during the powered portion of SSR ascent. The program takes in the time series data containing ambient air temperature, ambient air density, and rocket velocity. These time series are produced by the program **Rocket.m**, which was described in Sec. 2.

Equation (6.9) is used to calculate stagnation point heat flux. Equation (6.28) is used to calculate the heat flux on the rocket nose cone caused by turbulent flow. All of the aforementioned fluxes are functions of the local rocket wall temperature. The program finds wall temperatures at the stagnation point and several points on rocket nose such that the absorbed heat flux is equal to the heat flux radiated away. These temperatures are determined for all time intervals during the rocket's powered ascent.

Equation (6.25) is used to calculate the heat flux on the rocket cylinder base caused by the turbulent flow. The cylinder does not radiate away any of absorbed heat. Being a heat sink shield, it absorbs the heat and gets hotter. The program calculates the cylinder base temperature at the end of the powered flight.

So, the program **ThermalAnalysis.m** performs calculations for rocket heating. The results of these calculations are presented in Subsection 6.4.

6.2 Thermal Protection Systems

There are three categories of heat shields. These are **radiative shields**, **ablative shields**, and **heat sink shields**. **Radiative shields**, which radiate away almost all of the heat flux they receive. They conduct almost no heat. SSR nose cone uses a radiative heat shield. **Ablative shields** absorb the heat flux. The heat is dissipated by pyrolysis and sublimation of the shield material [78, p.80]. SSR does not use ablative heat shields anywhere. **Heat sink shields** absorb heat flux. These shields generally consist of light metals which can absorb considerable thermal energy without becoming extremely hot. SSR cylinder rocket uses Aluminum 6061 T6 cylinder wall as a "natural" heat shield. During the rocket flight the wall experience heating, but not enough to become dysfunctional.

6.2.1 Radiative Heat Shields

A typical radiative heat shield consists of three layers. The outermost layer is composed of a thin metal sheet. The metal should be resistant to oxidation and have high **emissivity**. Emissivity is the "ratio of the radiant flux emitted per unit area to that of an ideal black body at the same temperature" [43, p.2-45]. The next layer is flexible thermal insulation composed of ceramic fiber. The innermost layer is the underlying rigid structure. This is the shield used on SSR nose cone. In some works, the whole three layer shield is called a **metal heat shield** [95].

Outermost Layer – Oxidation Resistant Metals

The outermost layer of the metal heat shield is subject to both high heat flux and hypersonic oncoming wind. This layer must have high melting point and high oxidation resistance. Oxidation

resistance of material is defined in terms of its recession rate under the influence of high temperature oxidizing environment. The recession rate depends on material, temperature, air density, and oncoming wind velocity. In some cases, recession follows a linear law:

$$d_r(t) = K_{\text{linear}} t, \tag{6.29}$$

where $d_r(t)$ is the recession distance, t is the exposure time, and K_{linear} is a linear recession constant. The constant K_{linear} has units of m/s. Some oxidation-resistant metals are protected from oxidation by an outer oxide layer [96]. This layer is protective for temperatures beyond the oxide melting point. For instance, refractory metals such as tungsten and molybdenum have poor oxidation resistance due to the low melting points of their corresponding oxides. In cases where metal oxide does provide protection, metal recession follows a parabolic law:

$$d_r(t) = \left(K_{\text{parabolic}} t\right)^{1/2}, \tag{6.30}$$

where $d_r(t)$ is the recession distance, t is the exposure time, and $K_{\text{parabolic}}$ is a parabolic recession constant. The constant $K_{\text{parabolic}}$ has units of m^2/s.

For temperatures up to 1,300 ^{o}C, Nickel has good oxidation resistance. In static air at atmospheric pressure and 1,300 ^{o}C temperature, it has parabolic oxidation rate with constant $K_{\text{parabolic}} = 2.5 \cdot 10^{-15}\ m^2/s$ [96]. Under these conditions, it takes 10,000 seconds to oxidize a layer of nickel 0.005 *mm* thick. Inconel's oxidation resistance is slightly lower. In static air at atmospheric pressure and 1,300 ^{o}C temperature, it has parabolic oxidation rate with constant $K_{\text{parabolic}} = 7 \cdot 10^{-14}\ m^2/s$ [97, p.19]. Nickel and Inconel with oxidised surface have emissivity of at least 0.75 [98, p.52], [99, p.E-386]. Inconel 625 sheets 0.5 *mm* thick are available at $380 per m^2 [100]. These sheets have areal density of 4.2 kg/m^2. An alloy containing 80% Nickel and 20% chromium has excellent properties and can be multiply reused as heat shield up to 1,200 ^{o}C [95, p.1]. The oxidized surface of the alloy has emissivity of 0.7 to 0.9 [101, p.184]. In static air at atmospheric pressure and 1,300 ^{o}C temperature, the alloy has parabolic oxidation rate with constant $K_{\text{parabolic}} < 2 \cdot 10^{-15}\ m^2/s$ [101, p.207].

Chromium is oxidation-resistant up to 1,550 ^{o}C [102]. A layer of chromium oxide protects chromium from rapid oxidation at high temperatures [103]. Pure chromium should have been protected by its oxide up to its melting point of about 1,900 ^{o}C. Unfortunately, the Cr_2O_3 forms eutectic with lower oxides and melts away at 1,650 ^{o}C [102]. In air at atmospheric pressure and 1,550 ^{o}C temperature, chromium has parabolic oxidation rate with constant $K_{\text{parabolic}} = 1 \cdot 10^{-12}\ m^2/s$ [104, 105].

More expensive metals and alloys are needed to provide oxidation protection at higher temperatures [106, 107, 108, 109, 110, 111]. For SSR nose cone, however, Nickel, Inconel, and Chromium are sufficient.

Second Layer – High Temperature Thermal Insulation

Relatively inexpensive ceramic felt and cloth thermal isolation is available. CeramFiber thermal insulation works up to 1,260 ^{o}C. A sheet weighing 3 kg/m^2 costs $58 per m^2 [112]. Superwool HT Paper 2 *mm* thick has areal density of 0.45 kg/m^2, thermal conductivity below 0.25 $W/(m\,^oK)$,

and good properties up to 1,300 ^{o}C [113, p.46]. Zirconia Grade ceramic fiber paper works up to 1,420 ^{o}C. A sheet weighing 3 kg/m^2 costs \$147 per m^2 [114]. Flexible ceramic fiber blankets can serve as heat insulation up to 1,420 ^{o}C [115] as well. All the aforementioned fibers can resist temperatures 100 ^{o}C higher than their classification for about a minute.

Zircar Zirconia produces Yttria Stabilized Zirconia fiber and felt. Zirconia felt works up to 2,000 ^{o} C [116]. Zirconia cloth works up to 2,200 ^{o} C [117].

SSR Thermal Insulation

SSR nosecone has a simple radiative heat shield. The stagnation point and the first 10 *cm* of the cone are covered by a 1 *mm* thick chromium sheet. The second layer at that area consists of a 1 *cm* thick Zirconia Grade ceramic fiber paper. This combination can withstand temperatures of up to 1,520 ^{o}C which is 1,793 ^{o}K for duration of SRS ascent. The emissivity of oxidized chromium surface is at least 0.6 [99, p.E-387]. Thus, this section of heat shield can handle heat fluxes up to

$$\dot{Q} = e_w \sigma_B T_w^4 = 3.6 \cdot 10^5 \frac{W}{m^2}, \tag{6.31}$$

where $\sigma_B = 5.67 \cdot 10^{-8}\ W/m^2K^4$ is the Stefan–Boltzmann constant.

The rest of the nose cone is covered by a 0.5 *mm* thick nickel or Inconel sheet. The second layer consists of CeramFiber blanket 1 *cm* thick. This shield section can withstand temperatures of up to 1,260 ^{o}C which is 1,533 ^{o}K. The emissivity of oxidized Inconel surface is at least 0.75 [99, p.E-387]. Thus, this heat shield can handle heat fluxes up to

$$\dot{Q} = e_w \sigma_B T_w^4 = 2.35 \cdot 10^5 \frac{W}{m^2}, \tag{6.32}$$

As we see in Subsection 6.4, the heat flux on SSR cone never reaches such value at any point.

6.2.2 Heat Sink Shields

The heat sink shield consists of three layers similar to metal radiative heat shield. The outermost layer is composed of metal. The next layer is flexible thermal insulation composed of ceramic fiber. The innermost layer is the underlying rigid structure. The difference between heat sink shield and radiative heat shield is the function of the outer layer. Whereas the outer layer of the radiative heat shield radiates away the heat flux, the outer layer of heat sink shield absorbs the thermal energy. Heat sink shields are most useful for absorbing short and powerful heat fluxes. These shields have been used for suborbital vehicles since 1950s [118, p.23].

Natural heat sink shield does not occur in nature. It is a part of a rocket or aircraft which has another primary function and also fulfils an extra function as a heat shield. For instance, a military aircraft may have armor which can act as a heat sink shield during short-time supersonic maneuvers. A solid rocket's metal shell mainly serves to contain the pressure of fuel grain combustion product. This shell may serve as a natural heat sink shield as long as it does not overheat during hypersonic flight.

SSR has such natural heat sink shield. As we mentioned in Section 5.2, the rocket cylinder

consists of a 0.5 *cm* thick aluminum wall. Below we calculate the heat load such wall can withstand.

Rocket cylinder wall can be heated only so far as it retains tensile strength to hold the solid rocket motor. Aluminum 6061 T6 is the material composing the artillery rocket cylinder wall. It's yield strength is 283 *MPa* at -28 ^{o}C, 276 *MPa* at 24 ^{o}C, 262 *MPa* at 100 ^oC, 250 *MPa* at 118 ^oC, and 214 *MPa* at 149 ^oC. On further heating, it rapidly loses strength [119, 47]. Aluminum 7075 or Duralumin, another prospective cylinder wall material, retains 95% of yield strength up to 100 ^{o} C. Then its strength falls rapidly [120].

It takes 73 J/g to heat aluminum from 20 ^{o}C to 100 ^{o}C [43, p. 12-190]. The 0.5 cm thick aluminum wall has an areal density of 13.5 kg/m^2. During the rocket motor burning, it can absorb a heat flux of

$$73\,\frac{J}{g}\times 1.35\cdot 10^4\,\frac{g}{m^2}=9.9\cdot 10^5\,\frac{J}{m^2}. \tag{6.33}$$

As we show in Subsection 6.4, the heat flux at cylinder base is under 1 MJ/m^2 unless the firing altitude is 12 *km* and rocket burning time is under 50 *s*. In this case, the rocket may have to be covered with a light outer heat shield.

Long-range rockets fired from the ground sustain an order of magnitude higher heat load. These rockets must have extensive outer heat shields. This is one of the reasons such rockets are expensive [79, p. 103-106].

6.3 SSR Heating

In this subsection we estimate the maximal heat load on various parts of the artillery rocket (SSR) during its' ascent. The 30 *cm* SSR is described in great detail in Section 3.4. In this Subsection we describe the heating of three parts of SSR: the stagnation point, the nose cone and the rocket cylinder. The nose cone experiences greater heat flux than the rocket cylinder. Counterintuitive as it is, some parts of the nose cone experience greater heat flux than the stagnation point. The steps in heat flux calculations for the three parts are somewhat different.

The three parts of SSR have different heat shields. Both SSR stagnation point and SSR nose cone use a radiative heat shield described in Subsection 6.3. The temperature of this shield at any moment depends on the local heat flux. SSR cylinder uses a natural heat sink shield described in Subsection 6.3. The temperature of this shield grows slowly almost in proportion to the absorbed heat load. SSR outer shell containing the three aforementioned parts is presented below:

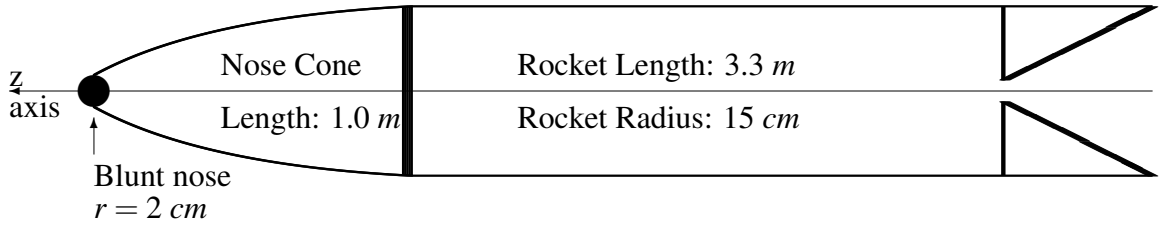

Figure 12: Artillery rocket outer shell

6.3.1 SSR Stagnation Point

During the rocket ascent, SSR stagnation point experiences laminar flow heating. The heat flux is given by (6.9). This heat is radiated away at the rate given by

$$\dot{Q}_S^{\gamma} = e_w \sigma_B T_w^4, \tag{6.34}$$

where $\sigma_B = 5.67 \cdot 10^{-8}\ W/m^2K^4$ is the Stefan–Boltzmann constant, and $e_w < 1$ is the wall emissivity. The program **ThermalAnalysis.m** calculates the temperature for which the incoming heat flux is the same as heat flux radiated away. This calculation is done for every point on SSR trajectory.

6.3.2 SSR Nose Cone

In order to calculate the heat flux, we must visualize the nose cone:

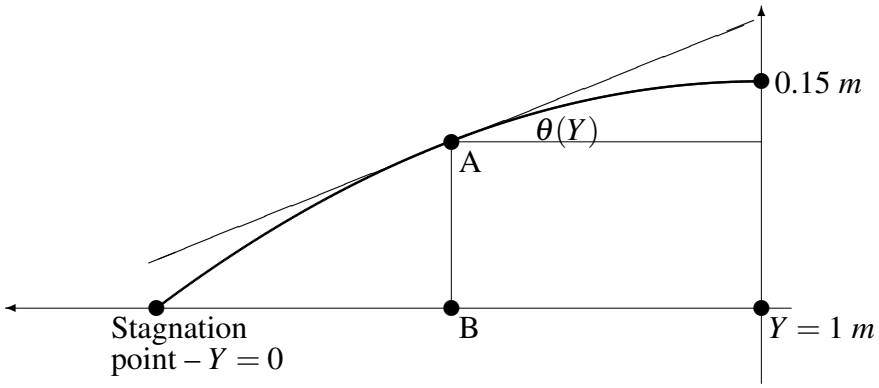

Figure 13: Nose cone

Any point A on the cone can be located in terms of an angular coordinate $\phi \in [0, 2\,\pi)$ and a non-angular coordinate Y. If B is the projection of A onto Y axis then Y is the distance between A and the stagnation point. Heat flux and heat shield temperature are independent of ϕ due to the angular symmetry. Below, we calculate the heat flux and the heat shield temperature for several values of Y.

For an ogive cone with radius 0.15 m and length 1.0 m, the inclination of any plane segment at coordinate Y is

$$\theta(Y) \approx 0.3 \cdot \frac{1\ m - Y}{1\ m}. \tag{6.35}$$

The turbulent flow heating rate is given by (6.28). The heat is radiated away at the rate given by (6.34). The program **ThermalAnalysis.m** calculates the temperature for which the incoming heat flux is the same as heat flux radiated away. This calculation is done for every point on SSR trajectory. The heat shield temperatures for SSR rocket for different firing altitudes, initial velocities, and rocket firing times are shown in Figure 14 below.

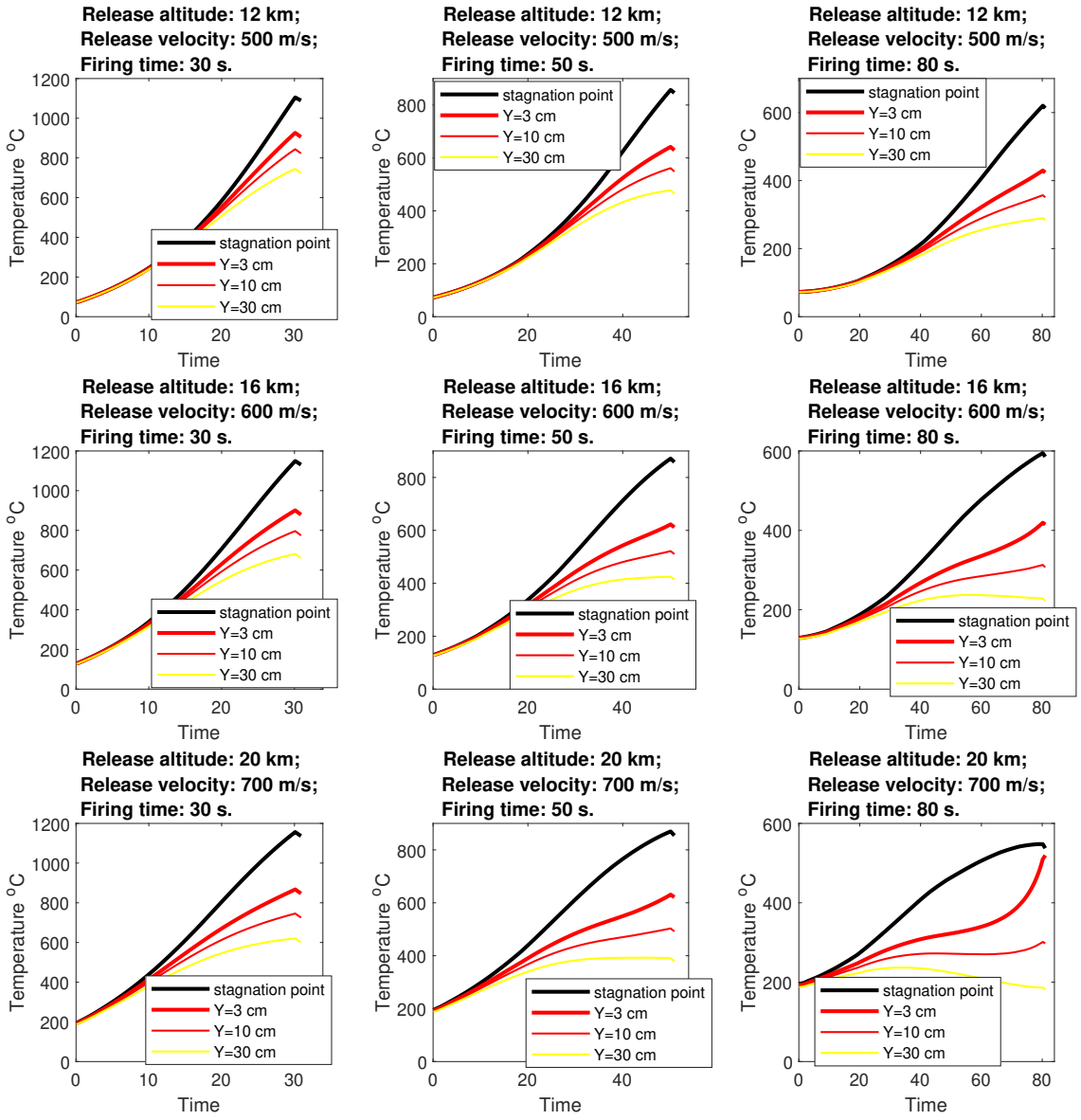

Figure 14: Aerodynamic heating of SSR nose cone

All of the maximum temperatures are within the capabilities of three-layered radiative heat shields described in Subsection 6.3.

6.3.3 SSR Cylinder

The turbulent flow heating rate is given by (6.28). All the heat is absorbed by the 0.5 *cm* thick aluminum rocket body. Almost no heat is radiated away. Assuming SSR body starts out at 20 ^{o}C, the program **ThermalAnalysis.m** calculates how much the rocket body heats up during the motor firing. After firing, the rocket body may absorb more heat, but it will have no effect on rocket performance. The temperature of the rocket cylinder base after firing is tabulated in Table 17.

Firing time	30 s	40 s	50 s	60 s	80 s
$H = 12\ km$, $v = 500\ m/s$	94 ^{o}C	81 ^{o}C	68 ^{o}C	58 ^{o}C	47 ^{o}C
$H = 16\ km$, $v = 600\ m/s$	75 ^{o}C	66 ^{o}C	59 ^{o}C	55 ^{o}C	46 ^{o}C
$H = 20\ km$, $v = 700\ m/s$	61 ^{o}C	56 ^{o}C	52 ^{o}C	48 ^{o}C	43 ^{o}C

Table 17: Rocket cylinder base heating

For combinations of rocket altitude, velocity, and firing time, rocket cylinder heating presents no problem.

7 Conclusion and Further Considerations

7.1 Conclusion

In this work we have demonstrated the feasibility of a rocket artillery system consisting of a RLA and SSR. The RLA is a vertical takeoff vertical landing (VTVL) vehicle making the whole system relatively compact. RLA never approaches the target closer than 220 km making it much less vulnerable to anti-aircraft weapons than modern fighters and bombers.

The cost of delivery of munitions by the SSR should be much lower than the cost of delivery of munitions by modern theatre ballistic missiles (TBM). This is the case due to the greatly reduced requirements placed on the SSR compared to TBM. First, SSR require much lower $\triangle v$ than TBM. Second, SSR can burn fuel over 80 s which is much slower than most modern TBMs. Third, as we have shown in Subsection 6.2, the SSR reach high velocity in high stratosphere and experience only moderate heating.

In Subsection 5.1, we have calculated the weight of munition a RLA with an empty mass of 4,500 kg and total mass of 10,000 kg can carry. The aforementioned RLA can release four 300 kg SSR at an altitude of 12 km and the speed of 500 m/s. Alternatively, RLA can release two 300 kg SSR and a lighter 200 kg rocket at an altitude of 16 km and the speed of 600 m/s. RLA can also release two 200 kg rockets or one regular 300 kg SSR at an altitude of 16 km and the speed of 700 m/s.

A SSR having an initial mass of 300 kg can deliver a 60 kg charge to the target. The charge can consist of one or more projectiles. The ranges and impact velocities for a warhead containing four Europrojectiles are listed in Table 16.

7.2 Variations and Alternatives for Artillery Rockets with Reusable First Stage

There are many feasible designs of rocket artillery with reusable first stage. In this work we have described a system consisting of the RLA and SSR. This system may have several varying parameters. First, the takeoff mass of RLA may vary considerably. The fuelled RLA may be a 3-ton drone or a 200-ton heavy rocket bomber. Second, the type of rocket engine may vary – it may be a solid propellant engine, a liquid propellant engine, or a hybrid. Liquid propellant engines will have lower fuel costs and higher engine costs. Solid propellant engines will have higher fuel

costs and lower engine costs. Third, there are many choices of fuel, oxidizer, and a wide range of possible fuel-oxidizer mass ratios. They would have to be cost-optimized for desired performance. Forth, there are many types of reusable engines producing given thrust. Different engines have different chamber pressures and expansion ratios. High chamber pressure improves performance but increases the engine cost. Fifth, there are many types of airframes and different airframe materials. Some materials are vastly superior to duralumin, but their cost is also extremely high. American fifth-generation fighters are very high performance aircraft, but their cost is also very high. For instance, American fifth-generation fighter F35 has a unit cost of $90 Million [121].

Other designs for artillery rockets with reusable first stage should be considered. One concept is reusable rocket with discarding fuel and oxidizer tanks presented in Figure 15 below:

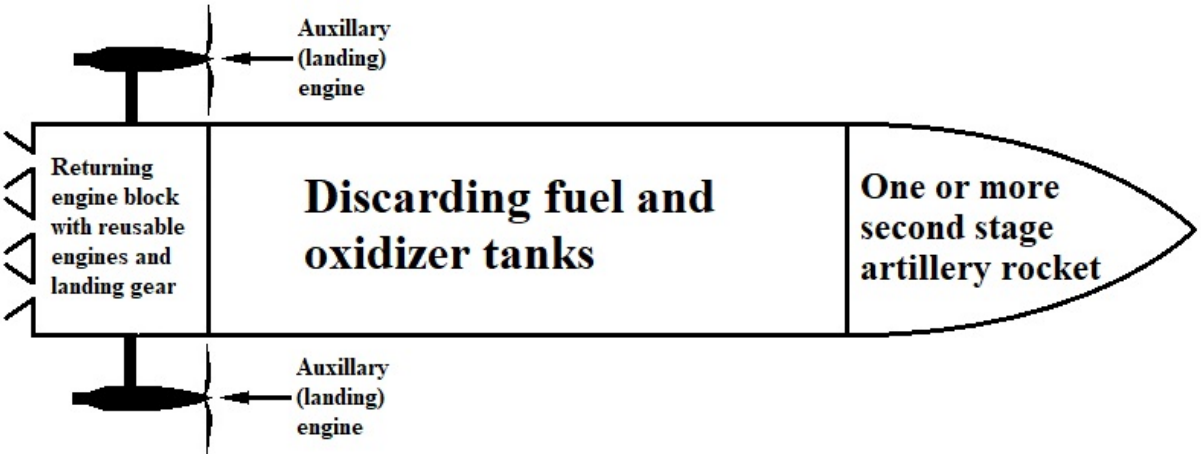

Figure 15: Reusable rocket with discarding tanks

This system may have some advantages over RLA. The propellant mass fraction for this system may be much higher than that of RLA. As defined in Subsection 5.1, propellant mass fraction f_p, is the quotient of mass of propellant used for liftoff and initial acceleration to gross liftoff mass. We estimate f_p by estimating the mass fractions of other elements and subtracting them from 1. The mass fraction of SSRs with their containers is 0.12. That is the secondary rocket mass fraction of 0.08 given for Sortie B of Subsection 5.1 plus mass fraction of 0.04 for rocket container. The mass fraction for the engine block with fuel used for return and landing should be 0.2. We estimate this number based on the general thrust-to-weight ratio of 70 for rocket engines [34, p.3]. The mass fraction for discarding tanks should be 0.12 [122]. Subtracting these numbers from 1, we obtain $p_f = 0.56$, which is higher than the propellant mass fraction for any of the sorties described in Subsection 5.1. Higher p_f would enable the SSRs to be released at a greater altitude and greater initial velocity.

Reusable rocket technology has a rich and interesting future. This technology will be used in Space Exploration and Colonization. This technology will be used for sounding rockets and stratospheric scientific research. This technology will definitely be used by military.

References

[1] Perrimond, G., *1944–2001: The threat of theatre ballistic missiles,* Supplément à TTU Europe, 2002.

[2] Wood, J., *Russia, the Asymmetric Threat to the United States: A Potent Mixture of Energy and Missiles,* Santa Barbara, Calif: Praeger Security International, 2009.

[3] Parker, S., Pang, A., *The M270 Multiple Rocket Launcher,* Mankato, Minn: Capstone Press, 2008.

[4] *Procurement Programs, Department of Defense Budget Fiscal Year 2016*, Office of the Under Secretary of Defense, 2015

[5] Eshel, T., Israel Tests Sea-Launched LORA Missile, *Defense Update,* Jun 20, 2017, <http://defense-update.com/20170620_lora-2.html>, accessed March 7, 2018.

[6] Heginbotham, E., *The US-China Military Scorecard: Forces, Geography, and the Evolving Balance of Power, 1996-2017,* Santa Monica, California : RAND, 2015.

[7] US Department of Defense (DoD), *Annual Report to Congress: Military and Security Developments Involving the People's Republic of China,* Washington, DC, 2017.

[8] Wunderle, W.D., *US Army Weapons Systems 2009,* New York: Skyhorse Pub, 2008..

[9] Prenatt, J., Hook, A., *Katyusha: Russian Multiple Rocket Launchers 1941-Present,* London: Bloomsbury Publishing Place, 2016.

[10] AR3 Multiple Launch Rocket System, *Military-Today.com,* <http://www.military-today.com/artillery/ar3.htm>, accessed Jan 14, 2018.

[11] Turner, P. E., New and Evolving Armaments and Subsystems for Future Conflicts, *Precision Fires Rocket and Missile Systems*, 2016.

[12] Merkley, J. A., *Trident II Missiles: Capability, Costs, and Alternatives,* Washington, DC: Congress of the U.S., Congressional Budget Office, 1986.

[13] Gormley, D. M., *Dealing with the Threat of Cruise Missiles,* S.l.: Routledge, 2017.

[14] Technical tune to Agni test before talks, *Telegraph,* 2004.

[15] Watts, B.D., *Six Decades of Guided Munitions and Battle Networks: Progress and Prospects*, Center for Strategic and Budgetary Assessments, 2007.

[16] Tucker, S., *The Encyclopedia of Middle East Wars: The United States in the Persian Gulf, Afghanistan, and Iraq Conflicts.* Santa Barbara, Calif: ABC-CLIO, 2010.

[17] Bogan, J., Boeing boosts production of precision-guided bomb kits made in St. Charles to fight ongoing wars by air, *Saint Louis Today,* Jan. 27, 2017.

[18] Fresconi, F., Celmins, I., Silton, S. and Costello, M., High Maneuverability Projectile Flight Using Low Cost Components, *Aerospace Science and Technology,* **41**, p. 175-188, 2015.

[19] ATK's Precision Guidance Kit for artillery projectiles now approved for production, *Army Recognition,* 6 Feb., 2015.

[20] Gould, J., US Army 'Dumb' 155mm Rounds Get Smart, *Defense News*, March 13, 2015, http://www.defensenews.com/story/defense/land/weapons/2015/03/13/orbital-atk-wins-us-army-deal-for-pgk/70222932/.

[21] Foss, C. Smart ammo: precision-guided munitions for field artillery, *Jane's Defence Weekly,* 2015.

[22] Burke, P.G., Pergolizzi, A. XM1156 Precision Guidance Kit (PGK) Overview, *2010 Fuze Conference,* May, 2010.

[23] Biass, E.H., Compendium Artillery, *Armada*, **39**(2), April-May 2015.

[24] Orbital ATK Artillery Precision Guidance Kit Surpasses 10,000 Units Delivere, *Orbital ATK Inc.*, Press Release, February 2017.
<https://www.orbitalatk.com/news-room/PrinterFriendly.asp?prid=223>, accessed Jan 8, 2018.

[25] Forrester, A., Orbital ATK reaches milestone in M1156 Precision Guidance Kit production, *govconwire*, 2018.
<https://www.govconwire.com/2018/05/orbital-atk-reaches-milestone-in-m1156-precision-guidance-kit-production>, accessed June 9, 2019

[26] Wang, B., Israel Converts Artillery into a Precision Guided Weapons, *Next Big Future,* 2017.

[27] O'Rourke, R., *Navy Lasers, Railgun, and Hypervelocity Projectile: Background and Issues for Congress*, Congressional Research Service 7-5700, Nov., 2015.

[28] Cheatwood, F., Mohamed M., Ragab, A., Launch Vehicle Recovery and Reuse, *AIAA SPACE 2015 Conference and Exposition*, 2015.

[29] Woodward, D., *Space Launch Vehicle Design,* Dissertation at Department of Mechanical and Aerospace Engineering University of Texas at Arlington, 2017.

[30] de Selding, P.B., SpaceX's reusable Flacon 9: What are the real cost savings for customers?, *Space News*, 2016.

[31] New Glenn, *Blue Origin*,
<https://www.blueorigin.com/new-glenn/>
Accessed September 2, 2019.

[32] Grilliot, D., Hatch,C., Multiple Launch Rocket System (MLRS) Fuzing Evolving to Meet End User Requirements, *51st Annual NDIA FuzeConference,* KDI Precision Products, Inc., 2007.

[33] Tsiolkovski, K. and M K. Tikhonravov, M.K., *Works on Rocket Technology,* Washington, D.C.: National Aeronautics and Space Administration, 1965.

[34] Biblarz, O., Sutton, G.P., *Rocket Propulsion Elements, Eighth Edition,* John Wiley & Sons, Inc., 2010.

[35] Jain, S.R., Oommen, C., Ammonium nitrate: a promising rocket propellant oxidizer, *Journal of Hazardous Materials,* **67**(3), p. 253-281, 1999.

[36] Kumar, P., Effect of catalysts on the burning rate of phase stabilized ammonium nitrate based composite propellants, *IOP Conference Series: Materials Science and Engineering*, 2018.

[37] Caveny, L.H., Felsheim, C.R., Summerfield, M., *Burning Rate Measurement of Thin Sheets of Double Base Prpopellant,* Princeton University, 1975.

[38] Ponomarenko, I.A., *Rocket Propulsion Analysis,* V 1.2.6, Lite Edition 2011, Cologne, Germany, 2011.
<http://www.propulsion-analysis.com>

[39] Brewster, Q., Ishihara, A., Sheridan, T., Ammonium nitrate-magnesium propellant combustion and heat transfer mechanisms, *Journal of Propulsion and Power,* **2**(4), p. 760-769, 1992.

[40] Azuma,Y., Murata, H., Simoda, M., Tohara, T., Effect of magnalium (Mg-Al alloy) on combustion characteristics of ammonium nitrate-based solid propellant, *Science and Technology of Energetic Materials,* **61**(2), p. 58–66, 2000.

[41] Northam, G.B., *Effects of Propellant Composition Variables on Acceleration-Induced Burning-Rate Augmentation of Solid Propellants,* NASA Langley Research Center Hampton, 1972.

[42] Lengellé,G., Duterque, J., Trubert, J.F., *Combustion of Solid Propellants,* Research Scientists, Energetics Department Office national détudes et de recherches aérospatiales (ONERA), France, 2004.

[43] Lide, D. R., Editor, *CRC Handbook of Chemistry and Physics,* 84th Edition, CRC Press. Boca Raton, Florida, 2003.

[44] Kubota, N., *Propellants and Explosives,* WILEY-VCH Verlag GmbH & Co. KGaA, Weinheim, 2007.

[45] Bell, G.C., Stamm, D.C., MDA Booster Cost Analysis, *Joint ISPA/SCEA Annual Conference,* June 24 – 27 2008.

[46] OnlineMetals.com, Web, <https://www.onlinemetals.com/>, Accessed May 14, 2019.

[47] Aluminum 6061-T6; 6061-T651, *MatWeb, Your Source for Materials Information,* <http://www.matweb.com/SpecificMaterial.asp?bassnum=MA6061t6>, Accessed September 4, 2019.

[48] Innovation in Composite CNG Cylinders, *JEC Asia 2009 Automotive & Mass Transport Forum,* Owens Corning, 2009.

[49] *Report on CNG Cylinders for Automotive Vehicle Applications,* Ashok Leyland Ltd, Chennai, 2012.

[50] Ventura, M.C., Long Term Storability of Hydrogen Peroxide, *41st AIAA/ASME/SAE/ASEE Joint Propulsion Conference,* 2005.

[51] Heister, S., Ventura, M., Wernimont, E., Steve Yuan, S., Rocket Grade Hydrogen Peroxide (RGHP) for use in Propulsion and Power Devices - Historical Discussion of Hazards, *43rd AIAA/ASME/SAE/ASEE Joint Propulsion Conference,* 2007.

[52] Chhibber, R., Kulkarni, S.G., Panda, S.P., Prabhakaran, C. Rocket Performance of Red Fuming Nitric Acid with Blends of Norbornadiene, Carene and Cardanol, *Defence Science Journal,* **42**(3), p. 165-171, 1992.

[53] Florczuk, W., Rarata, G., Novel Liquid Compounds as Hypergolic Propellants With HTP, *Journal of KONES Powertrain and Transport,* **23**(1), 2016.

[54] Melof, B.M., Grubelich, M.C., Investigation of Hypergolic Fuels with Hydrogen Peroxide, 37th AIAA / ASME / SAE / ASEE Joint Propulsion Conference and Exhibit Salt Lake City, Utah, 8-11 July 2001.

[55] Davis, S.M., Yilmaz, N., Advances in Hypergolic Propellants: Ignition, Hydrazine, and Hydrogen Peroxide Research, *Advances in Aerospace Engineering,* Volume 2014, Article ID 729313, 2014.

[56] Maschio, L. J., Marques, R. I., Meyer, W. M., Pereira, L. G. F., Vieira, R, A DOE study on the hypergolicity of hydrogen peroxide with a rocket liquid fuel based on monoethanolamine and ethanol, *International Journal of Energetic Materials and Chemical Propulsion,* **17**(2), p.137-145, 2018.

[57] *Code of Practice Nitrous Oxide,* European Industrial Gases Association AISBL, 2007.

[58] CCM: China's market price of furfural bounces back in April, *China Chemicals,* 2016.

[59] Price and market trends: Europe ethanolamines stable to firm, *ECA*, <https://www.icis.com/explore/resources/news/2016/09/09/10032659/price-and-market-trends-europe-ethanolamines-stable-to-firm/> Accessed June 16, 2019

[60] Trafton, A., New method for synthesizing the epoxides found in plastics, textiles, and pharmaceuticals could be powered by electricity, MIT News, 2019.

[61] Min-hee, J. Does Falling Ethylene Price Signal the End of the Chemical Industry Boom, *buisnesskorea.co.kr*, Dec 19, 2018.

[62] Ghedini, E., Menegazzo, F., Signoretto, M., Strukul, G., Looking for the “Dream Catalyst" for Hydrogen Peroxide Production from Hydrogen and Oxygen, *Catalysts,* **9**(251), 2019.

[63] Product Profile: Hydrogen Peroxide, *ChemArc,* India, <https://www.chemarc.com/feed/article/product-profile–hydrogen-peroxide/5b15268bef00a4214070ce7a>
Accessed June 26,2019.

[64] *Hydrogen Peroxide Handbook,* Chemical and Material Sciences Department Research Division Rocketdyne, a Division of North American Aviation, Inc., Canoga Park, California, 1967.

[65] Renck, T., NHRA nitro teams talk about the rising cost of nitromethane, *Competition Plus*, Accessed Feb 15, 2019.

[66] Topchiev, A.V., *Nitration of Hydrocarbons and Other Organic Compounds,* Pergamon Press, 1959.

[67] Burris, J.J., *A Study of the Gas Phase Nitration of Natural Gas,* Thesis, University of Alberta, Edmonton, 1946.

[68] *Nitrous Express,*
https://www.nitrousexpress.com/customer-service-faqs.html
Accessed June 16,2019

[69] El-Sayed, A.F., *Fundamentals of Aircraft and Rocket Propulsion,* Springer-Verlag London 2016.

[70] Luidens, R. W., Weber, R. J., An Analysis of Air-turborocket Engine Performance Including Effects of Component Changes, *NACA Research Memorandums,* 1956.

[71] Siuru, W.D., Holder, W.G., *General Dynamics F-16 Fighting Falcon,* Fallbrook, CA: Aero Publishers, 1983.

[72] Gordon, Y., Davison, P., *Mikoyan Gurevich MiG-29 Fulcrum,* North Branch, Minnesota: Specialty Press, 2005.

[73] Gordon, E., Komissarov, D., *Mikoyan Mig-29 & Mig-35,* 2019.

[74] Rogers, C. E. and Cooper, D., RASAero II, *Rocket Aerodynamic Analysis and Flight Simulation Software,* V 1.0.1. 2016, Rogers Aeroscience, Lancaster, CA, 2016.

[75] Hundertmark, S. and Lancelle, D., A Scenario for a Future European Shipboard Railgun, *17th Int. Symposium on Electromag. Launch Tech. (EML)*, arXiv:1410.2496v1, 10/9/2014.

[76] Crowell, G.A. *The Descriptive Geometry of Nose Cone,* Scribd, 1996, http://www.scribd.com/doc/60921375/

[77] Ott, D. E., *Field Artillery, 1954-1973,* Department of the Army, Washington, D.C., 1975.

[78] Akin, D.L., Entry Aerothermodynamics, Slides from *2012 NASA Thermal and Fluids Analysis Workshop,* <https://tfaws.nasa.gov/TFAWS12/Proceedings/Aerothermodynamics%20Course.pdf>, Accessed Aug 15, 2019.

[79] Fleeman, E. L., *Tactical Missile Design.* Educational series, AIAA, Reston, VA, 2001.

[80] Clancy, L. J., *Aerodynamics,* Pitman Publ. Lim., London, 1975.

[81] Tauber, M. E., *A review of High-Speed, Convective, Heat-Transfer Computation Methods,* NASA Technical Paper 2914, Ames Research Center, 1989.

[82] Sutton, K. Graves, R.A., A General Stagnation Point Convective Heating Equation for Arbitrary Gas Mixtures, *NASA TR-R-376,* 1971.

[83] Chapman, G.T., Theoretical Laminar Convective Heat Transfer & Boundary Layer Characteristics on Cones at Speeds to 24 km/s, *NASA TN D-2463,* 1964.

[84] Detra, R.W., Hidalgo, H., Generalized heat transfer formulas and graphs for nose cone re-entry into the atmosphere, *ARS Journal,* **31**(3), p. 318–321, 1961.

[85] Shubov, M.A., Shubov, M.V., Aerodynamic performance of ultra-long range projectiles, *Mathematics in Engineering, Science and Aerospace,* **8**(1), p. 3-27, 2017.

[86] Brown, R.L., Das, K., Cizmas, P.G.A., Whitcomb, J.D., *A Numerical Investigation of Actively Cooled Structures in Hypersonic Flow,* Texas A&M University, College Station, TX, 77843-3141.

[87] Kemp, N. H., Rose, P. H., Detra, R. W., Laminar Heat Transfer Around Blunt Bodies in Dissociated Air, *Journal of the Aero/Space Sciences,* **26**(7), p. 421-430, 1959.

[88] Mouradlan, R.M., Theraal Analysis of SNAP-10A Reactor Core During At Bospheric Reentry and Resulting Core Disintegration, *Atomics International, Report NAA-SR-TDR-11847,* 1966.

[89] Lienhard, J. IV, Lienhard, J. V, *A Heat Transfer Textbook, Third Edition,* Cambridge, Massachussets, 2001.

[90] Gottlieb, J.J., Ritzel, D.V., *A Semi-Empirical Equation for the Viscosity of Air,* Suffield Technical Note No. 454, Defence Research Establishment Suffield Ralston Alberta, 1979.

[91] Higgins, K., Comparison of Engineering Correlations for Predicting Heat Transfer in Zero-pressure-gradient Compressible Boundary Layers with CFD and Experimental Data, *Defence Science and Technology Organisation,* 2008.
<http://www.dsto.defence.gov.au/corporate/reports/DSTO-TR-2159.pdf>,
Accessed September 11, 2019.

[92] Kulfan, R.M., *Historic Background on Flat Plate Turbulent Flow Skin Friction and Boundary Layer Growth,* HSR Airframe Technical Review, 1998.

[93] Trinh K.T., Tuoc, K., On The Critical Reynolds Number For Transition From Laminar To Turbulent Flow, *arXiv preprint arXiv:1007.0810,* 2010.

[94] Crabtree, L.F., Dommett, R.L., Woodley, J.G., *Estimation of Heat Transfer to Flat Plates, Cones and Blunt Bodies,* Aeronautical Research Council Reports and Memoranda, R. & M. No. 3637, London: Her Mmjesty's Stationery Office, 1970.

[95] Johnson, R., Killpatrick, D. H., *Evaluation of Dispersion Strengthened Nickel – Base Alloy Heat Shields for Space Shuttle Application,* National Aeronautics and Space Adminstration, Washington, D. C., 1976.

[96] Haugsrud, R., On the high-temperature oxidation of nickel, *Corrosion Science,* **45**(1), p. 211-235, 2003.

[97] Finfrock, C.C., Greene, G.A., *Oxidation of Inconel 718 in Air at Temperatures From 973 K to 1620 K,* Energy Sciences and Technology Department, Brookhaven National Laboratory, 2000.

[98] Kaye, G.W.C., Laby, T.H., *Tables of Physical and Chemical Constants,* 15th Edition, Longman, London, 1986.

[99] Astle, M.J., Weast, R.C., *CRC Handbook of Chemistry and Physics,* 63rd Edition, CRC Press, Boca Raton, Florida, 2003.

[100] "0.02" Nickel 625 Sheet", *OnlineMetals.com,* 2019,
<https://www.onlinemetals.com>,
September 19, 2019.

[101] Johnson, R., Killpatrick, D. H., *Evaluation of Dispersion Strengthened Nickel – Base Alloy Heat Shields for Space Shuttle Application, Phase 1 Summary Report* National Aeronautics and Space Adminstration, Washington, D. C., 1973.

[102] Scruggs, D. M., Modified Chromium for Unprotected Structures, *ARS Journal,* **31**(11), p. 1527-1533, 1961.

[103] Opeka, M.M., Talmy, I.G., Zaykoski, J.A., Oxidation-based materials selection for 2000 ^{o}C+ hypersonic aerosurfaces: Theoretical considerations and historical experience, *Journal of Materials Science,* **39**(19), p.5887-5904, 2004.

[104] Hallström, S., Halvarsson, M., Höglund, L., Jonsson, T., Ågren, J., High temperature oxidation of chromium: Kinetic modeling and microstructural investigation, *Solid State Ionics,* **240**, p.41-50, 2013.

[105] Hagel, W.C., Seybolt, A.U., Cation Diffusion in Cr2O3, *Journal of The Electrochemical Society,* **108**(12), p.1146-1152, 1961.

[106] Dickinson, C.D., Seigle, L.L., *Experimental Study of Factors Controlling the Effectiveness of High-Temperature Protective Coatings for Tungsten,* Technical Documentary Report No. ASD-TDR-63-774, Defense Documentation Center for Scientific and Technical Information Cameron Station, Alexandria, Virginia, 1964.

[107] *Summary of the Tenth Meeting of the Refractory Composites Working Group,* Defense Metals Information Center, Battelle Memorial Institute Columbus 1, Ohio, 1965.

[108] Krier, C.A., *Coatings for the Protection of Refractory Metals From Oxidation,* Defense Metals Information Center, Battelle Memorial Institute Columbus 1, Ohio, 1961

[109] *High-Temperature Oxidation-Resistant Coatings: Coatings for Protection From Oxidation of Superalloys, Refractory Metals, and Graphite,* Committee on Coatings, National Materials Advisory Board, Division of Engineering, National Research Council, 1970.

[110] White, J.E, Development of Oxidation-Resistant Tungsten-Base Alloys, *AIAA Journal,* **4**(2), 1966.

[111] Bai, M., Smith, M., Sun, W., et. al., Ablation-resistant carbide $Zr_{0.8}Ti_{0.2}C_{0.74}B_{0.26}$ for oxidizing environments up to 3,000 ^{o}C, *Nature Communications,* 14 Jun 2017.

[112] Ceramfiber, Ceramic Fiber Blanket by ceramafiber, *Amazon,* 2019,
<https://www.amazon.com/ceramafiber-Ceramic-Fiber-Blanket-Insulation/dp/B0771QNP3G/>,
September 19, 2019.

[113] *Product Data Book,* Thermal Ceramics is a business of Morgan Advanced Materials, 2018,
<http://www.morganthermalceramics.com/>,
Accessed September 6, 2019.

[114] CeramicFiberOnline, Ceramic Fiber Paper Zirconia Grade, *CeramicFiberOnline,* 2019
<https://www.ceramicfiberonline.com/product/ceramic-fiber-paper-552-108240125/>,
September 1, 2019.

[115] Ceramic Fiber Blanket, *Celsius Heat Management,* Belgium, 2018,
<http://www.celsius-group.com/>,
Accessed September 6, 2019.

[116] High Temperature Yttria Stabilized Zirconia Felt, Zircar Zirconia, Inc., 2018,
<http://www.zircarzirconia.com>, Accessed September 1, 2019.

[117] High Temperature Yttria Stabilized Woven Zirconia Cloth, Zircar Zirconia, Inc., 2018, <http://www.zircarzirconia.com>, Accessed September 1, 2019.

[118] Jenkins, D.R., Launius, R.D., *Coming home: reentry and recovery from space,* US Government Printing Office, 2011.

[119] High-Strength Super High Precision Aluminum Alloy Plate for Precision Machining, Kobe Steel, LTD., 2013,
<http://www.kobelco.co.jp>, Accessed September 4, 2019.

[120] Miracle, D., Senkov, O., Senkova, S., Cryogenic and elevated temperature strengths of an Al-Zn-Mg-Cu alloy modified with Sc and Zr, *Metallurgical and Materials Transactions A,* **37**(12), p. 3569-3575, 2006.

[121] Pentagon and Lockheed Martin Agree To Reduced F-35 Price in New Production Contract, *F-35 Lightning II Program,* Public Release, 2018.

[122] Pietrobon, S.S., Analysis of Propellant Tank Masses, *NASA*, 2009.